nature cell biology

ARTICLES

https://doi.org/10.1038/s41556-021-00713-x

Check for updates

Dynamin-dependent vesicle twist at the final stage of clathrin-mediated endocytosis

Xiaodong Cheng[1,2,4], Kuangcai Chen[1,4], Bin Dong[1,4], Meek Yang[1], Seth L. Filbrun[1], Yong Myoung[1], Teng-Xiang Huang[1], Yan Gu[3], Gufeng Wang[1]✉ and Ning Fang[1,2]✉

Dynamin has an important role in clathrin-mediated endocytosis by cutting the neck of nascent vesicles from the cell membrane. Here, using gold nanorods as cargos to image dynamin action during live clathrin-mediated endocytosis, we show that, near the peak of dynamin accumulation, the cargo-containing vesicles always exhibit abrupt, right-handed rotations that finish in a short time (~0.28 s). The large and quick twist, herein named the super twist, is the result of the coordinated dynamin helix action upon GTP hydrolysis. After the super twist, the rotational freedom of the vesicle increases substantially, accompanied by simultaneous or delayed translational movement, indicating that it detaches from the cell membrane. These observations suggest that dynamin-mediated scission involves a large torque generated by the coordinated actions of multiple dynamins in the helix, which is the main driving force for vesicle scission.

Dynamin is a GTP-binding protein that participates in various membrane fission and fusion processes[1–6], including clathrin-mediated endocytosis (CME). At the final stage of CME, dynamin assembles and acts as a mechanochemical scaffold that constricts and deforms the membrane at the neck of invaginated clathrin coated pits (CCPs) and cuts the nascent vesicles from the cell membrane[7–9]. There is a growing consensus as to the roles that dynamin has during the fission process:[10] (1) dynamin self-assembles into helices around a lipid membrane tube; (2) GTP-bound dynamin favours more constricted states of the helix; (3) vesicle fission is induced by the dynamin helix in a GTP hydrolysis-dependent manner. However, how dynamin breaks the neck of the CCPs is still under debate.

Currently, two prevailing models have been proposed. (1) The two-stage model[11–16], which suggests that, during the first stage, dynamin in a nucleotide-bound conformation assembles into a helical structure, leading to a constricted membrane tube inside. During the second stage, coordinated GTP hydrolysis by multiple dynamin molecules facilitates the formation of a hemi-fission intermediate of the membrane tube and destabilizes the dynamin assembly, followed by the rupture of the membrane tube. Structural studies showed that, during GTP hydrolysis, the relative orientation between the GTPase and bundle signalling element portions in dynamin changes by ~70° (refs. [17,18]). This conformational change may be transmitted through the stalk, leading to a tilted Pleckstrin homology domain and the wedging of the lipid membrane underneath[15,19]. With this strong interaction, the energy barrier for hemi-fission to occur diminishes or even disappears[12,20].

(2) The ratchet/constriction model[9,21,22]. In this model, dynamin can act as a molecular motor, similar to myosin. The model suggests that, when assembled, adjacent rungs slide on each other progressively after cycles of stochastic GTP hydrolysis, leading to the twisting and constriction of the helix until the membrane tube reaches a state in which the hemi-fission intermediate can form spontaneously or through thermal fluctuation. Finally, disassembly of the dynamin helix is proposed to be caused either by conformational stress as the transition state conformation cannot be docked in any of the dynamin helical structures[17], or by loss of the underlying membrane tube template due to fission. This model is consistent with the in vitro observation that the dynamin helix generates a twisting motion after GTP hydrolysis[9]. The observed 70° rotation between the GTPase and the bundle signalling element portions is also consistent with this model, as it may cause a power-stroke that slides dynamin by one unit along the helix[17,19].

Both models include a crucial conformation change by assembled dynamins after GTP hydrolysis but the mechanochemical step has different purposes in scission. Recent theoretical studies suggest that the two models may be reconciled: an effective rotation of the dynamin helix around its longitudinal axis may happen simultaneously with the tilting of dynamin Pleckstrin homology domains, which better facilitates severing of the membrane energetically[23].

To resolve these issues and define the mechanism of dynamin-catalysed fission, it is important to directly observe dynamin action during the live endocytic process. Live-cell observation is especially crucial because dynamin may behave differently depending on its environment. For example, in the absence of the GTP, dynamin assembles into non-constricted, long helical coils around membrane tubes in vitro[7,24–26]. The addition of GTP generates torsion and constriction but may not necessarily cut the tube. By contrast, in the constant presence of GTP, which is more relevant to in vivo environment, dynamin will generate highly constricted but short helices that lead to scission[13]. In addition, the non-constricted helix of dynamin with no nucleotide has a one-start helical structure, whereas helices of dynamin assembled with nucleotides or analogues can have a one-start (that is, the constricted)[27] or a two-start (that is, the super-constricted) helical structure[19,28]. The one-start and two-start helical structures cannot convert to each other through sliding or simple reorganization[19,28], which brings into question which of these intermediate structures are relevant to dynamin action in vivo. All of these indicate that in vitro

[1]Department of Chemistry, Georgia State University, Atlanta, GA, USA. [2]State Key Laboratory of Physical Chemistry of Solid Surfaces, Innovation Laboratory for Sciences and Technologies of Energy Materials of Fujian Province (IKKEM), College of Chemistry and Chemical Engineering, Xiamen University, Xiamen, China. [3]The Bristol-Myers Squibb Company, Devens, MA, USA. [4]These authors contributed equally: Xiaodong Cheng, Kuangcai Chen, Bin Dong. ✉e-mail: gufengwang2011@gmail.com; nfang@gsu.edu

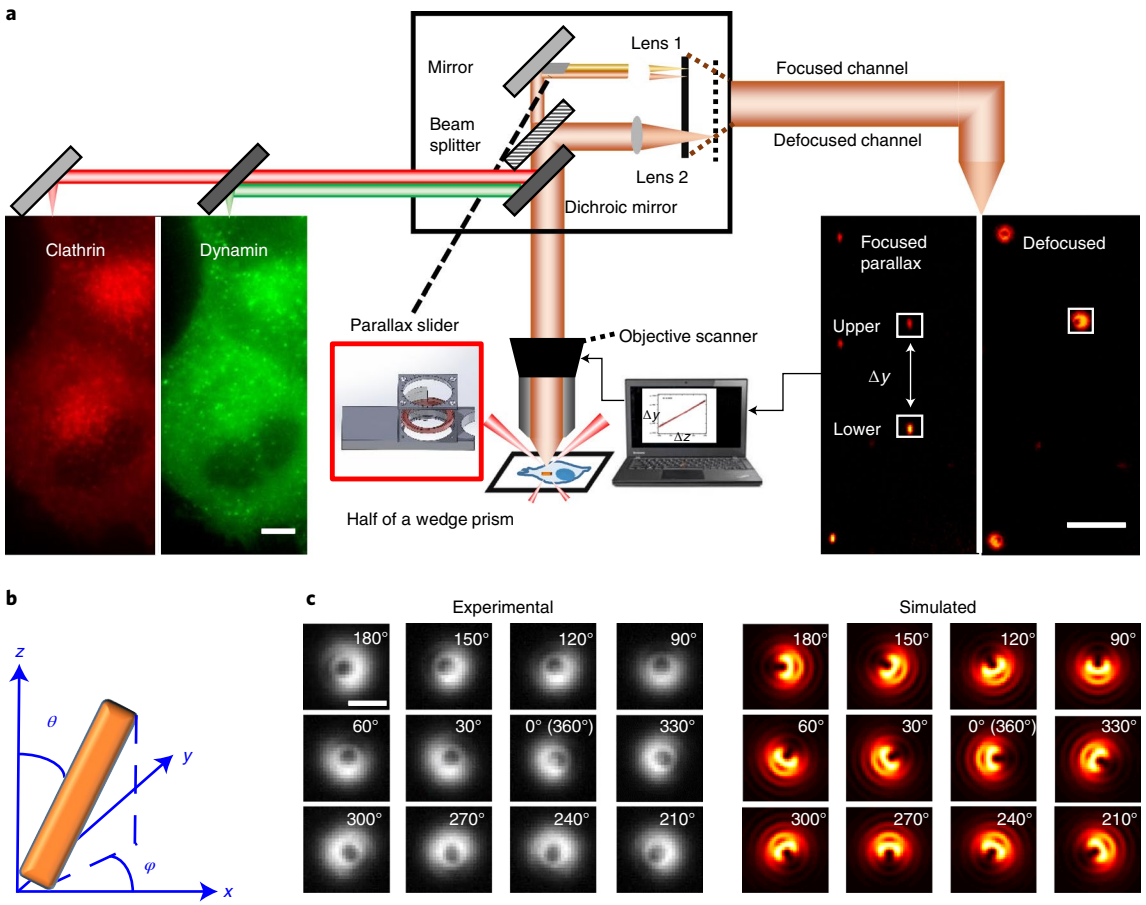

Fig. 1 | Scheme of 3D-SPORT. a, Schematic of the instrument. Scale bars, 5 μm. **b**, For the 3D orientation, θ is the polar angle and φ is the azimuth angle. **c**, Experimental (left) and simulated (right) defocused images of a AuNR with a fixed polar angle at different azimuth angles. In the experimental images, an AuNR was immobilized in agarose gel with a fixed polar angle of 60° and varying azimuth angles (indicated on the images) (more experimental images are shown in Extended Data Fig. 2). To recover their 3D orientation, a correlation coefficient mapping method was used, which compares an experimental image with all of the simulated images at different orientations, followed by a weighting procedure to report the most probable azimuth and polar angles of the probe. The simulated image patterns were from the theoretical point spread functions (PSF) of an emitting dipole, which were a function of its azimuth and polar angles and can be generated using the six basic functions of dipole emission (I_x^2, I_{xy}, I_y^2, I_{xz}, I_z^2, I_{yz}) (Supplementary Information 1.3 and Extended Data Fig. 3). These basic image patterns are dependent on system-specific parameters, including the numerical aperture and magnification of the objective, as well as the defocusing distance. The analysis of the orientation-dependent uncertainties associated with the recovered azimuth and polar angles is provided in Extended Data Fig. 4 and Supplementary Information 1.4. Importantly, the defocused image patterns are unique at different azimuth/polar angles, confirming that the defocused imaging overcomes angular degeneracy (with exceptions at a polar angle of ~90°, at which the azimuth angle shows a twofold degeneracy) (Supplementary Information 1.5) and provides true rotational direction information. For **c**, scale bar, 1 μm.

models may not apply to in vivo conditions and, therefore, live-cell observation is crucial in decoding how dynamin works.

Herein, we used gold nanorods (AuNRs)[29] as cargos and in vivo probes to directly report dynamin actions, especially the twisting behaviour, if there is any, during the complete endocytic process. AuNRs strongly scatter light at their localized surface plasmon resonance wavelengths, which is polarized along their axes, allowing them to be detected in the crowded cellular environment. The challenge for observing the rotational movement of these probes is that they are too small to resolve their orientation using conventional optical microscopy due to the optical diffraction limit. With our developed three-dimensional single-particle orientation and rotational tracking (3D-SPORT) system, it becomes possible to not only track the AuNR's translational movement in 3D space (focused channel; Fig. 1a) but also resolve its orientation changes (defocused channel; Fig. 1a).

Results

3D-SPORT. The essential aspect of this study is to use AuNR cargos to track changes in the orientation of cargo-laden CCPs during endocytosis in vivo and therefore measure the hypothesized twisting motions that are involved in dynamin-induced fission. To facilitate the CME of AuNRs, transferrin molecules were conjugated to the surface of 40 nm × 80 nm AuNRs. Gold nanoparticles with similar sizes modified in this way have been shown to be taken up by cells predominately through CME[30–33]. Well-dispersed nanoparticles in this size are endocytosed individually. They are tightly wrapped by the lipid membrane and their motions reflect the movement of the whole vesicle[32,34]. Given the size of these particles, we anticipate that each CCP and nascent clathrin-coated vesicle will carry only a single transferrin-conjugated AuNR and, therefore, their dynamics will report those of the cargo-laden CCP/clathrin-coated vesicle[35].

To track the AuNR's orientation over the entire 3D space (0–360° azimuth angle and 0–90° polar angle), defocused dark-field imaging was used to collect the image pattern of AuNRs[36]. We used a parallax imaging set-up to track the AuNR's 3D position, and used a feedback loop that automatically locks the AuNR probe in the focal plane to overcome the probe moving problem (Fig. 1a, Extended Data Fig. 1a, Methods, and Supplementary Information 1.1 and 1.2).

The collected defocused images (Fig. 1b,c and Extended Data Fig. 2) were compared with simulated image patterns (Supplementary Information 1.3 and Extended Data Fig. 3 (6 basic functions of dipole emission)) to obtain the AuNR's orientation. The instrument can resolve the 3D orientation (defined in Fig. 1b) of the AuNRs with a time resolution of ~20 ms. Under our typical live-cell imaging conditions, a precision of <2° can be accomplished for most polar and azimuth angles with a signal-to-noise ratio of ~10 (Extended Data Fig. 4 and Supplementary Information 1.4). The degeneracy problem of AuNRs can be effectively eliminated when the particle rotates slowly (Supplementary Information 1.5). The AuNR's position in the 3D space can be recovered with a precision of ~4–6 nm laterally and 14 nm axially (Extended Data Fig. 1b–f and Supplementary Information 1.6).

Multidimensional tracking. 3D-SPORT can collect the translational and rotational motion of AuNR probes in the 3D space in focused and defocused channels, respectively. Our customized instrument (Fig. 1a) also allows two additional fluorescence colour channels to be simultaneously collected with a second EMCCD camera, which provides dynamic molecular information (that is, dynamin and clathrin in this study) around the AuNR probe with a signal integration time of 0.5 s or 1.5 s and a waiting time between frames of 0.5 s. Sparsely distributed frames over time were used to minimize photobleaching.

In the experiments, we used the SK-MEL-2 cell line, which was gene-edited to express red fluorescent protein (RFP)-tagged clathrin (CLTA–RFP) and enhanced green fluorescent protein (eGFP)-tagged dynamin 2 (eGFP–DNM2)[37]. The surface-modified AuNR solution was added to cells plated on a glass substrate. Once a AuNR landed on the curved cell membrane surface, the recording was started and continued until AuNR was detected inside the cell (as indicated by linear translocation of the cargo over a long distance in the cell). All channels, including AuNR scattering, dynamin and clathrin fluorescence, were synchronized and recorded simultaneously. Only one AuNR was monitored during each experiment. To exclude any unambiguity, we focused on endocytosis events in which both dynamin and clathrin were observable (Supplementary Video 1).

Figure 2 shows an example of an endocytic event with the AuNR probe's translational displacements and two fluorescence channels. The simultaneous fluorescence observations give detailed dynamics of the recruitment of these two proteins on the vesicles and the entry spot.

Rotational motions of AuNR cargos during endocytosis. When the rotational motion of the cargo is considered, new information of endocytosis can be obtained. Figure 3a shows a typical example of tracked endocytosis events (Extended Data Fig. 5 shows the cell images, clathrin and dynamin information for this example).

At first glance, the AuNRs showed complicated motional patterns, experiencing multiple rotation-immobilization cycles. However, when combined with molecular information from the fluorescence observation, these motions can be classified into characteristic stages. All of the endocytosed AuNR cargos (45/45) showed a sequential combination of these characteristic stages throughout the process, although in some cases individual stages were missing or repeated. These stages of characteristic rotational motions are delineated in Fig. 3 (more examples of complete endocytosis events are shown in Extended Data Figs. 6 and 7). Of these, stages A–C are more variable, and are therefore discussed only briefly here, while more detailed discussions are provided in Supplementary Information 1.7. However, the super twist observed before vesicle departure is invariant.

Stage A: gradual loss of rotational freedom. When AuNRs first attached onto the cell membrane, they showed active rotation accompanied by lateral diffusion. The translational and rotational freedoms of the AuNRs were lost gradually, with the AuNRs going back and forth between the active rotation and immobilized modes[38,39]. The accumulation, and presumably assembly, of clathrin is often deemed to be an indication that endocytosis has started, which can be observed in stage A with large variations in duration[5]. This stage, which usually lasts for minutes (~2 min for the example in Fig. 3), is not plotted in full in Fig. 3 for clarity. Extended Data Fig. 8 and Supplementary Video 2 show a typical example of active rotation of a AuNR on the cell membrane surface at this stage.

Stage B: dynamin accumulation step with rotation variability. This stage is highly variable in length of time (Fig. 3 and Extended Data Figs. 6 and 7) and in rotational freedoms. In 5 out of 45 cases, the AuNR cargos would maintain static during the whole period (Extended Data Fig. 7a,d). In other cases, the AuNR cargos would restore slow or fast random rotations intermittently (for example, 147.2–166.0 s in Fig. 3a). This stage is defined by the recruitment of dynamin to the underlying CCP (shaded light green fluorescence in the background of Fig. 3a,b; 147.2–166.0 s) towards its peak, although the kinetics and the extent of dynamin recruitment varied considerably (Fig. 3 and Extended Data Figs. 6 and 7), as has been reported by other groups[6,40]. At the end of this stage, which coincided with the peak of dynamin recruitment/assembly, the cargo vesicle would pause rotation for those showed rotation earlier. Stage B took 18.8 s for this specific example in Fig. 3, which is consistent with the literature reports of the time for dynamin recruitment[37,41].

Stage C: static period before the super twist. Stage B is invariably followed by a brief static period, or waiting time (stage C; Fig. 3c, 166.0–166.76 s), as if the vesicle went into a deadlock, or was waiting for a signal to restart motion. To accurately calculate the duration of stage C, only 40 cases with AuNR rotation in stage B were taken into account. Thus, the duration was 1.9 ± 1.5 s (Fig. 4a). This stage occurs at or near to the peak of dynamin recruitment and could correspond to a constricted coated pit, which has been identified biochemically and linked to dynamin assembly[11].

Stage D: a right-handed super twist induces membrane fission. The most dramatic and invariant (45/45) observation was the occurrence of a large and rapid right-handed, in-plane rotation(s) of the AuNR (stage D in Fig. 3b, in which case the AuNR rotated 204° in-plane from 166.76 to 167.22 s). During the whole period, the polar angle barely changed (Fig. 3b).

The average twisting angle for all of the observed cases was $130 \pm 56°$ and was finished in a very short time of 0.28 ± 0.18 s (Fig. 4b,c). Given their magnitude, we named these rotations the super twist in this manuscript. Supplementary Videos 3–5 show three examples of these super twists imaged in the defocused channel starting from the static period. A large portion of these super twists (33/45; Fig. 3 and Extended Data Fig. 7b–d) were finished in a clear single step, with the rest (12/45; Extended Data Fig. 6 and Fig. 7a) showing two steps. No more than two steps were identified. The total length of time from the end of stage B to the departure of the vesicle (stage F, discussed below), which encompassed the peak of dynamin recruitment (Fig. 3a), was short (1.68 s in this example).

The coincidence of the peak of dynamin accumulation and the super twist suggests that the super twist may be driven by dynamin hydrolysis of GTP and is the major factor for driving fission and dynamin disassembly. To test this hypothesis, we carried out a control study using cells expressing the K44A dynamin mutant, which is defective in GTPase activity. In single-particle observation experiments in these cells, no successful endocytosis event was observed ($n = 25$) with a sufficiently long observation time (tens of minutes). Although characteristic AuNR motions consistent with early stages

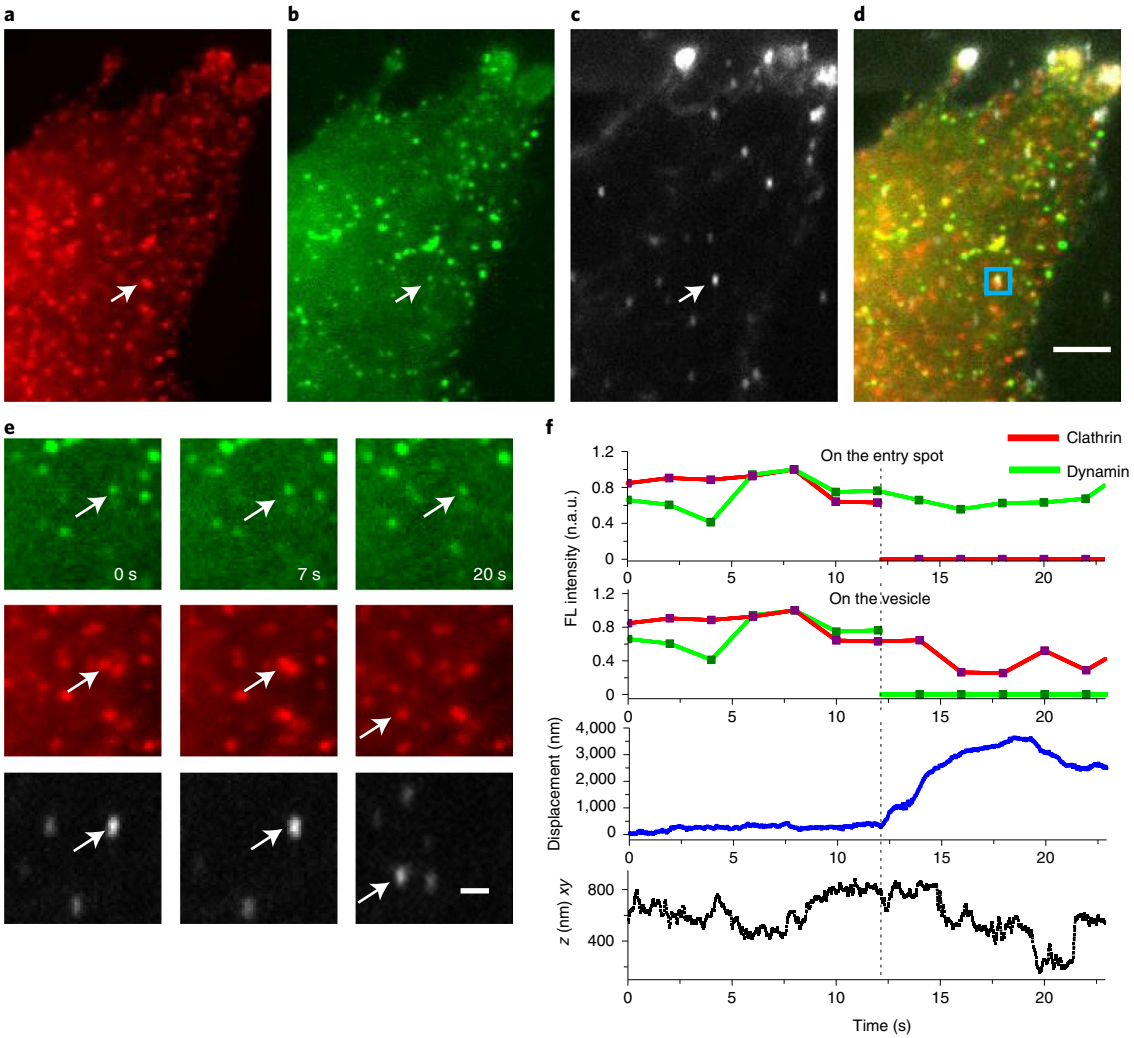

Fig. 2 | Multidimensional imaging of a AuNR and the surrounding molecular fluorescence. a, Clathrin channel. **b**, Dynamin channel. **c**, Focused scattering channel for AuNRs. The arrows in **a**–**c** indicate the overlap point of clathrin, dynamin and AuNR. **d**, Overlaid images. Scale bar, 5 μm (**a**–**d**). **e**, Magnified views of the region indicated by a square in **d** of the dynamin channel (top row), clathrin channel (middle row) and focused scattering channel (bottom row) at different times. The arrow pointed to the same cargo vesicle at different times in different detection channels. The colocalization of the scattering image of the AuNR cargo with clathrin and dynamin fluorescence provides direct evidence that CME happens for the observed endocytic event. Scale bar, 1 μm. **f**, Time evolution of clathrin and dynamin fluorescence (FL) on the entry spot, clathrin and dynamin fluorescence on the vesicle, and the lateral (*xy*) and axial (*z*) displacements of the particle from the entry spot during an endocytosis event. FL intensity (n.a.u.) represents normalized fluorescence intensity arbitrary units. The *z*-axis direction is defined as pointing towards the outside of the cell. The dashed line indicates the time of fission. The detachment of the nascent vesicle from the cell membrane occurred at 12.2 s, which was indicated in this case by a sudden large *xy*-displacement, accompanied by a 260-nm inward *z*-directional change from the original entry spot (**f**, bottom two panels). This indicates that fission happened at, or slightly before, the point at 12.2 s (that is, the detachment point). The accumulation of dynamin at the CCPs showed large variations from case to case but usually peaked around the detachment point. In this specific case, dynamin fluorescence on the vesicle quickly dropped to the baseline after fission; whereas the opposite was observed for clathrin fluorescence, which was lost from the entry spot, but remained on the vesicle for several seconds and dropped quickly to the baseline (**e** and **f**, top two panels). At the entry spot on the membrane, although the dynamin fluorescence persisted, the intensity dropped, possibly reflecting partial disassembly of the dynamin helix. Note that the focal plane moved away from the entry spot along with the vesicle, which also contributed, but to a lesser extent, to the fluorescence intensity drop at the entry spot (**f**). The experiment was performed five times with similar results obtained.

up to the static stage (stage C) were detected, no super twist was detected (Fig. 5a). These cells showed significantly reduced efficiency in internalizing AuNRs (Fig. 5b). As a result, CME was not completed. These data confirmed that the dynamin helix generates the super twist upon GTP hydrolysis.

Stage E: constrained random rotations before vesicle release. After the super twist, the vesicle had another period of relatively slow, random rotations within a limited range before the detachment from the cell membrane (stage E). The rotation steps ($10 \pm 13°$ per frame azimuth angle and $7 \pm 10°$ per frame polar angle; Fig. 6e,f) were larger than those in the first slow rotation stage B ($5 \pm 8°$ per frame azimuth and $3 \pm 6°$ per frame polar; Fig. 6c,d), yet much smaller than those in the random diffusion step (stage F: $21 \pm 32°$ per frame azimuth angle and $12 \pm 18°$ per frame polar angle; Fig. 6g,h). These observations possibly indicate that the rigid scaffold that stabilizes the vesicle and the neck was broken but the vesicle was still associated with the cell membrane through the remaining protein–protein interactions. The duration of this period was highly variable (2.1 ± 1.4 s; Fig. 4d).

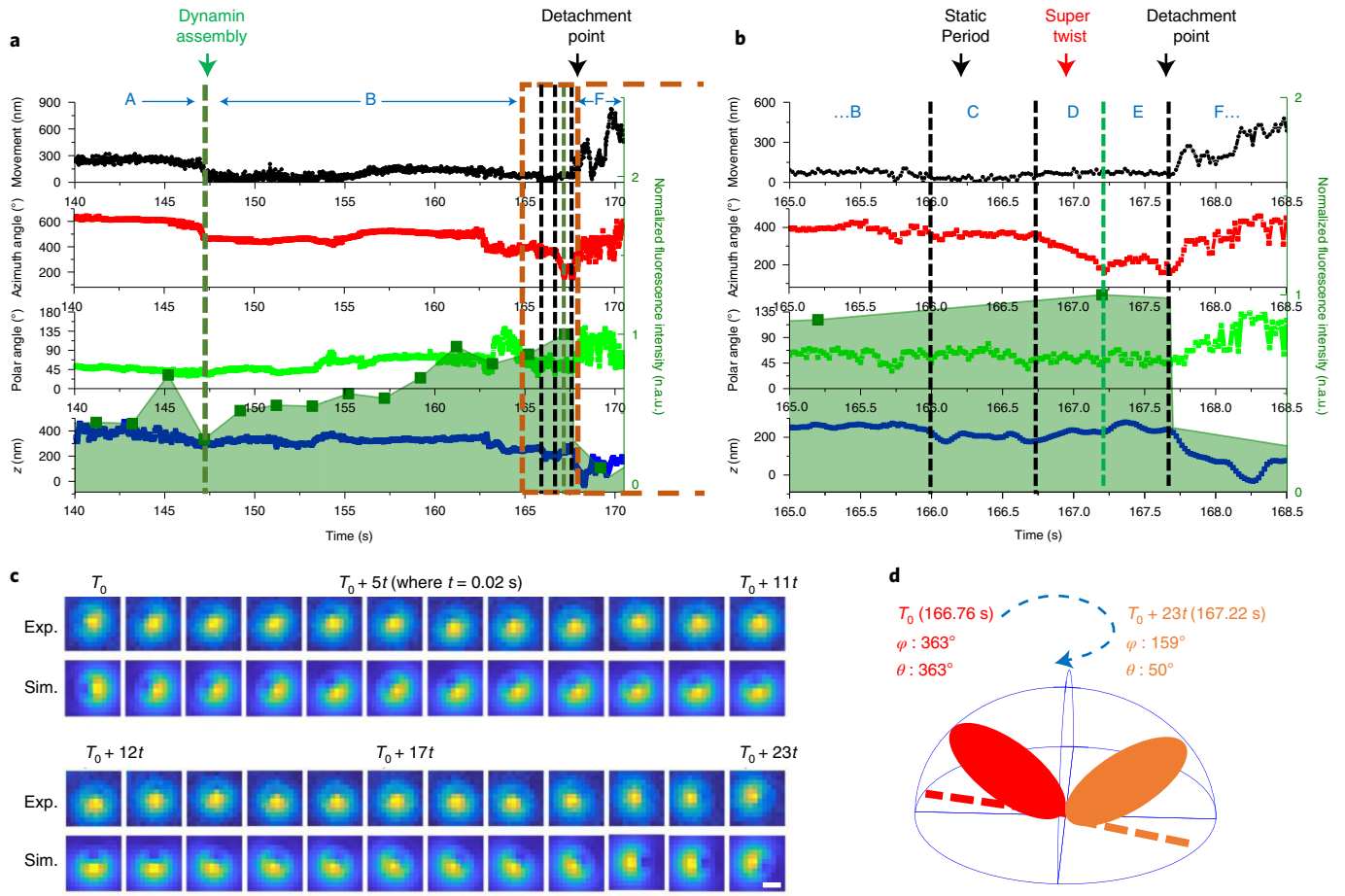

Fig. 3 | A typical example of an endocytic event with vesicle rotational information. a, The overlay of the time evolution of the cargo's *xy*-displacements, rotational azimuth, polar angles and *z*-displacement from top to bottom, and dynamin fluorescence is shown in the background (light green shading). Note that the azimuth and polar angles are cumulative with respect to the AuNR's initial orientation so that they may exceed their nominal ranges (0–360° and 0–180°, respectively). The movements can be interpreted in the context of dynamin fluorescence intensity, which is shaded light green in the background. The characteristic rotational motions together with fluorescence information can be delineated as the following 7 stages. A: the initial active rotation–immobilization cycles. B: the dynamin accumulation stage towards its peak with high variability in rotations. C: a static period before the super twist. D: the right-handed, super twist at the dynamin peak. E: a short, relatively slow random rotation period. F: a post-detachment period, which is characterized by either active translational and rotational diffusion, or linear transport with little rotation inside the cell. **b**, Expanded time window near the fission point (orange frame in **a**). **c**, The defocused image patterns of the cargo showing the super twist at stage D, t = 20 ms. Exp., experimental; Sim., simulated. Scale bar, 500 nm. **d**, Schematic of the AuNR's right-handed rotation during the super twist. The experiment was performed 45 times, with similar results obtained.

Stage F: vesicle detachment and severing point. The fission point, by convention, marks the time at which the vesicle membrane is no longer continuous with the plasma membrane. Pinpointing the fission point in live cells has been a challenging problem[41,42]. As we cannot exclude the possibility that a mature vesicle is still connected to the cell membrane through the protein scaffold, the fission point cannot be identified using conventional imaging methods.

Here, we use 'severing' or 'detachment' to describe the status of a mature vesicle that is no longer connected to the cell membrane by the lipid tube, or the rigid protein scaffold on the CCP neck. However, in practice, vesicles in this state may still be trapped in the actin mesh, or tethered to the membrane through loose connections such as actin filaments so they do not leave the entry spot immediately. Thus, the onset of the displacement cannot be used as the criteria for severing. Indeed, the disappearance of dynamin and/or clathrin fluorescence from the evanescent field as measured in total internal reflection fluorescence (TIRF) microscopy studies was shown to imprecisely reflect the scission point, as −7 ± 22 s from the point of the disappearance of the dynamin fluorescence in the evanescent field[40].

Our rotational observation can accurately determine the detachment point. A rigorous set of criteria was applied. First, our observations are based on dark-field imaging, which has a large depth of view and enables a more-complete assessment of the displacement of the cargo vesicle. A long-distance of diffusion or linear travelling provides definitive evidence that the cargo has entered the cell. Second, the most important criterium was the restoration of active rotational motions, which can be identified visually or through quantitative analysis. It happens slightly earlier than, or at the same time as, the onset of the lateral displacement. This criterium is used because a relatively rigid connection, either by the lipid membrane tube, or the remaining of the broken protein scaffold such as dynamin or other tightly bound coat proteins, would not allow large rotational steps (stage F: 21 ± 32° per frame azimuth angle, 12 ± 18° per frame polar angle (Fig. 6g,h), as opposed to stage B: 5 ± 8° per frame azimuth angle, 3 ± 6° per frame polar angle (Fig. 6c,d)). Third, in many events (~70%), the AuNR cargos had an instantaneous *z*-movement of >100 nm accompanied by the onset of the active rotation (for example, Fig. 3a at 167.7 s, which had an inward *z*-movement of 300 nm). The rapid *z*-movement is possibly

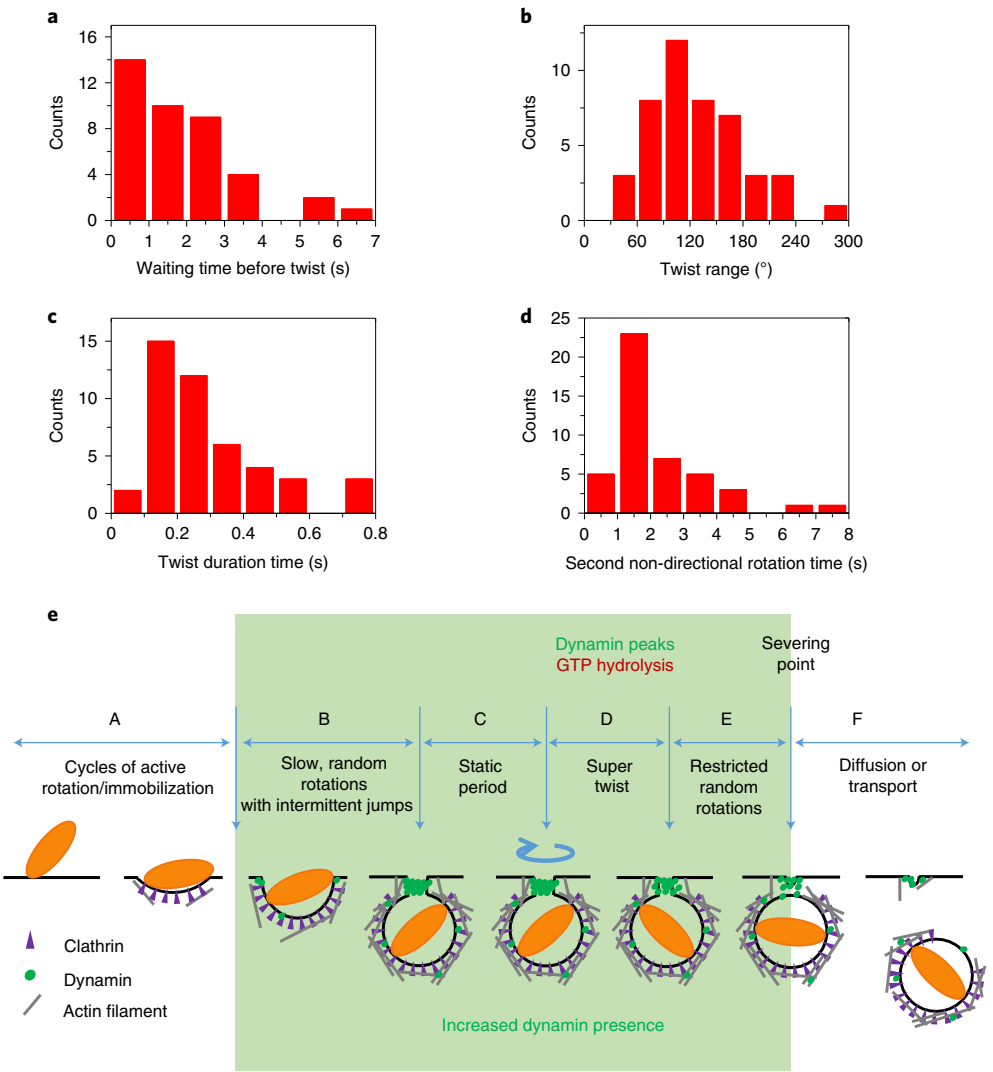

Fig. 4 | Statistics of the major events before fission and scheme of the dynamin scission model. a, The average waiting time before the super twist was 1.9 ± 1.5 s (stage C). Data are mean ± s.d. $n = 40$ biologically independent experiments. **b**, Distribution of the twisting angles with an average of 130 ± 56°. $n = 45$ biologically independent experiments. **c**, The average duration of the super twist was 0.28 ± 0.18 s (stage D). $n = 45$ biologically independent experiments. **d**, The average duration of the slow non-directional rotation time after the super twist and before fission was 2.1 ± 1.4 s (stage E). $n = 45$, biologically independent experiments. **e**, Scheme of the dynamin scission model. The endocytosis starts with the cargo's active rotational motion slowing down to complete immobilization (stage A). Clathrin accumulates during this stage. Then, a pulse of dynamin accumulation starts, initiating stage B. The cargo may restore intermittent slow or fast random rotations, or remain immobilized. For those cargos with restored rotational freedom, their rotation pauses (stage C) when dynamin accumulation peaks. GTP hydrolysis by assembled dynamin is then initiated either through an external trigger or simply by the completion of dynamin assembly, which generates a ~130° right-handed super twist (stage D). It is probable that the super twist leads to the hemi-fission of the membrane tube and the partial disassembly of the dynamin helix. Then, the cargo undergoes another period of relatively slow, constrained rotation (stage E), during which dynamin completely disassembles and scission completes. During the final stage (stage F), the vesicle is detached from the cell membrane. It either restores active random rotation and diffuses away, or is transported away by motor proteins.

caused by the release of tension that is generated by the rigid protein scaffold and other endocytic protein machinery after the severing of the vesicle from the membrane[43,44]. Finally, the recruitment dynamics of dynamin and clathrin on both the nascent vesicle and the entry spot facilitate the assignment of rotation stages (Figs. 2 and 3).

Determining the range of fission point. Although we were unable to determine the exact fission point, the existence of stage E possibly suggests that scission is a gradual process that involves the complete disassembling of proteins (for example, dynamin) that connect the vesicle and the cell membrane. The multidimensional approach used in our experiments enabled us to accurately pinpoint the time of vesicle detachment as well as the onset of the super twist. The fission point must occur after the start of the super twist, and before or at the point of vesicle detachment. Thus, we were able to narrow down the time range with a high level of confidence, that is, fission occurs within the range of 2.4 ± 1.5 s, encompassing the stages D and E.

Super-twist-like motion and abortive scission events. In the experiments, we also observed that dynamin accumulation/disassembly may happen without successful scission. Figure 7 shows such a case in which dynamin peaked at 75 s and disassembled in the following frames of images, without subsequent vesicle detachment. Although

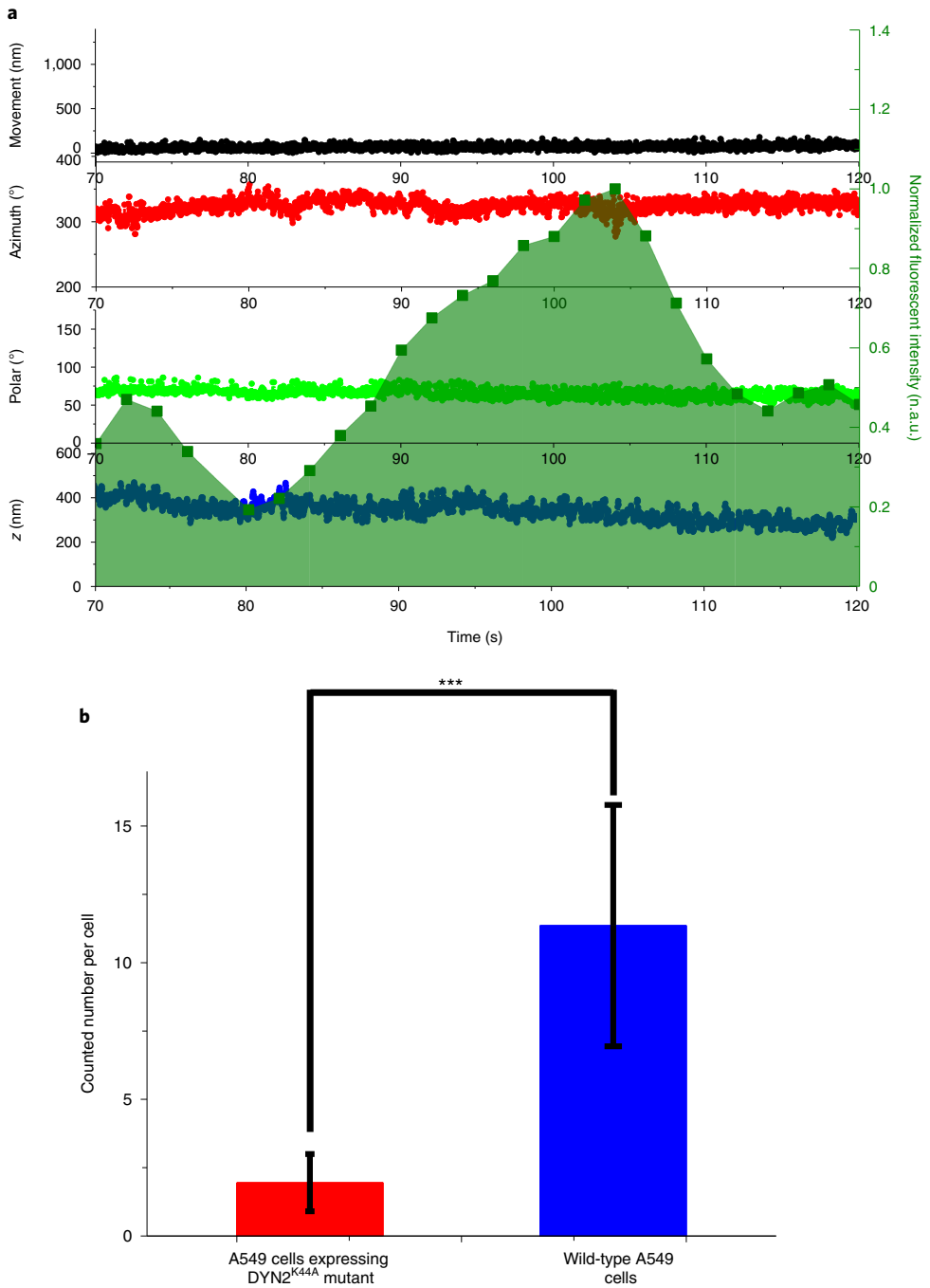

Fig. 5 | Endocytosis of AuNRs by A549 cells expressing K44A dynamin mutants with deficient GTPase activity. a, A typical example of a failed endocytosis event in an A549 cell expressing GFP-DNM2^{K44A}. The overlay of the time evolution of the cargo's *xy*- and *z*-displacements, rotational azimuth and polar angles, and dynamin fluorescence in the background. The experiments were performed 25 times with similar results obtained. **b**, AuNRs internalization efficiency. The internalized AuNRs after 2 h incubation time were counted for A549 cells expressing mutant DNM2^{K44A} and wild-type A549 cells. A549 cells expressing GFP-DNM2^{K44A}: 2.0 ± 1.0 per cell ($n = 42$ samples measured in 17 independent experiments). Wild-type A549 cells: 11.4 ± 4.4 per cell ($n = 41$ samples measured in 8 independent experiments). Data are mean ± s.d. Statistical analysis was performed using two tailed *t*-tests with unequal variance; the asterisks represent significant differences between the two groups; $^{***}P = 1.62 \times 10^{-17}$.

a smaller twist action of ~50° was detected, it failed to produce a large enough torque or twisting action to drive scission. These may represent failed scission attempts and we name these actions 'super-twist-like actions'. It is unclear why fission may fail, but a plausible explanation is that excessive resistance stalled the super twist. After the super-twist-like action, dynamin disassembled, possibly suggesting that the GTP hydrolysis leads to the disassembly of dynamin helix.

Discussion

The super twist. We report that, before scission, endocytic pits/vesicles invariably undergo a rapid super twist that coincides with the peak of dynamin recruitment and requires dynamin's GTPase activity in vivo. The twist unequivocally discloses that dynamin action generates a torque at the final stage of the scission.

This twisting action is partially consistent with the ratchet model, in which the GTPase domains of dynamin work as molecular

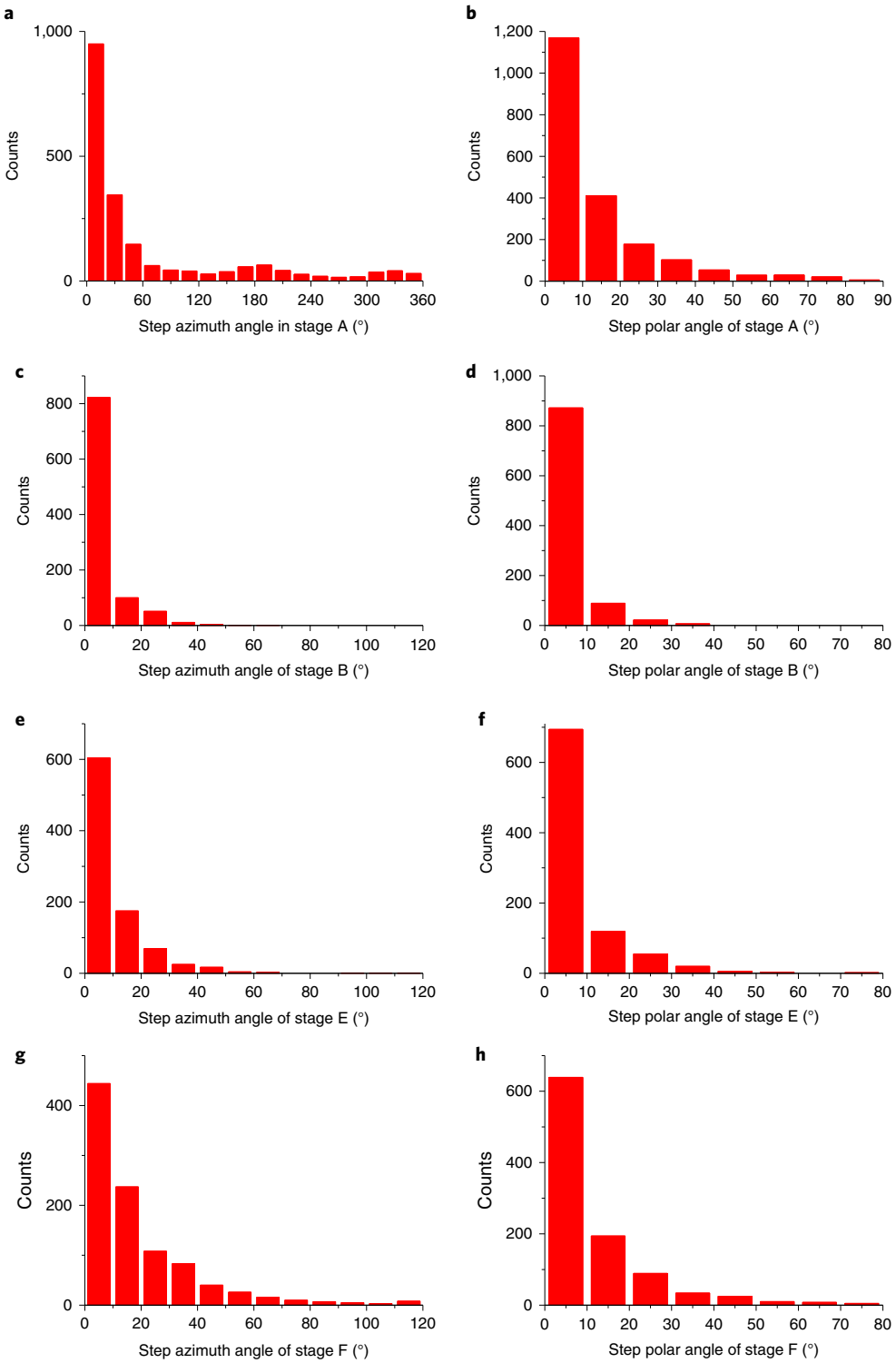

Fig. 6 | Rotation step sizes at different times during endocytosis. a,**c**,**e**,**g**, Azimuth steps. **b**,**d**,**f**,**h**, Polar steps. **a**,**b**, Stage A: active rotation after initial binding to cell membrane. Azimuth step size: 65 ± 92° per frame. Polar step size: 13 ± 16° per frame. Data are mean ± s.d. $n = 2{,}000$ steps measured in a representative experiment out of 45 independent repeats. **c**,**d**, Stage B: slow random rotations. Azimuth step size: 5 ± 8° per frame. Polar step size: 3 ± 6° per frame. Data are mean ± s.d. $n = 990$ steps measured in a representative experiment out of 45 independent repeats. **e**,**f**, Stage E: second random rotations after the super twist. Azimuth step size: 10 ± 13° per frame. Polar step size: 7 ± 10° per frame. Data are mean ± s.d. $n = 900$ steps measured across 8 independent experiments. The experiments were performed 45 times, with similar results obtained. **g**,**h**, Stage F: random diffusion after scission. Azimuth step size: 21 ± 32° per frame. Polar step size: 12 ± 18° per frame. Data are mean ± s.d. $n = 1{,}000$ steps measured across 12 independent experiments. The experiments were performed 45 times, with similar results obtained.

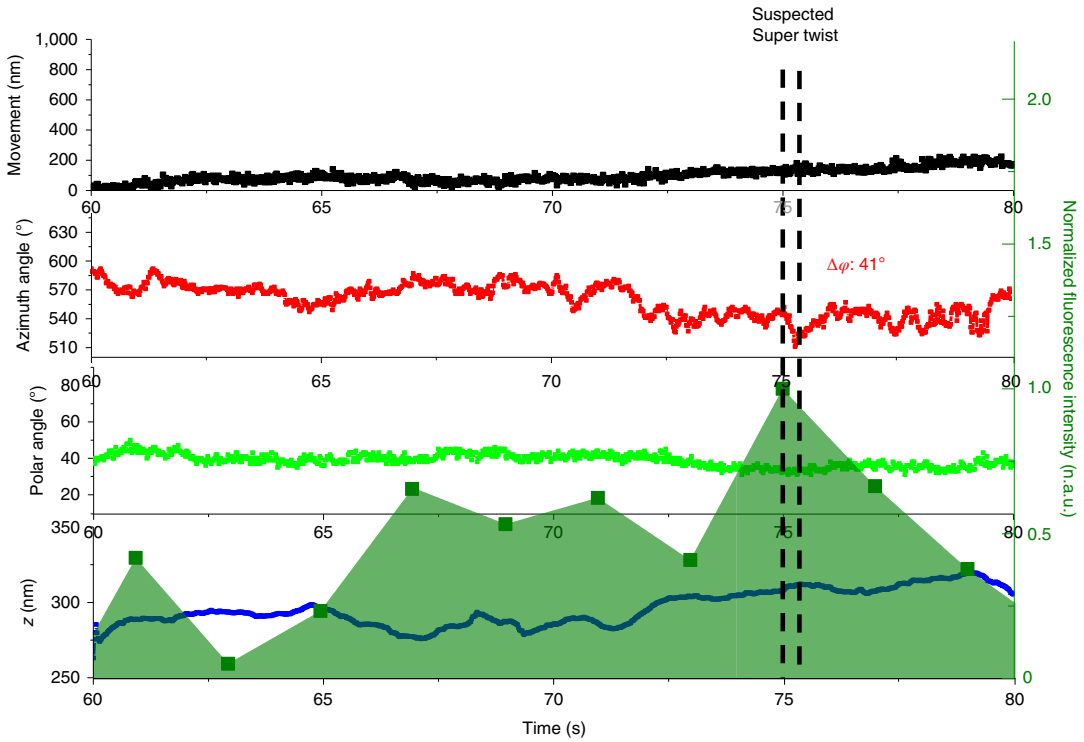

Fig. 7 | An example of an abortive scission event. The overlay of the time evolution of the cargo's *xy*-, *z*-displacements, rotational azimuth and polar angles, with dynamin fluorescence shown in the background. The experiments were performed four times with similar results obtained.

motors and slide on the helical turns by cycles of association–power stroke–dissociations, leading to the twisting and tightening of the membrane tube. However, the twisting occurs in an abrupt manner, and the whole process is finished in a very short time, ~0.28 ± 0.18 s (Fig. 4c), during which the cargo vesicle rotates by a large angle of 130 ± 56° (Fig. 4b) in the azimuth plane, with a peak rotation angle at ~130°. Given that the rate of assembly stimulated GTPase activity of dynamin is much slower[8], our data suggest that the super twist involves highly orchestrated conformational changes from multiple dynamin molecules.

It is unclear how constricted the dynamin assembly is before the super twist. Cryo-electron microscopy experiments have shown that the non-constricted helix composed of dynamin without nucleotides may have 14–18 dynamin dimers per rung[45,46], the constricted helix containing dynamin in the presence of GTP analogues has 13.2 dimers per rung[27] and the super constricted helix has a unique two-start structure and has 11.8 pairs of dynamin dimers per rung[19,28]. Assuming that the assembled dynamin before the super twist adopts a helical structure similar to one of the above-mentioned structures, a rotation of the vesicle by ~130° (around one-third of a circle) requires that the GTPase domain of dynamin slides by at least ~4 dynamin units along the helix. In the majority of these events (33/45), the super twist was completed in a single step in ~0.28 s. Considering that several GTP hydrolysis events are focused in such a short time, it suggests that this process involves coordinated actions from multiple dynamins in the helix, rather than independent, sequential GTP hydrolysis and twisting steps. Note that the focused GTP hydrolysis events are also consistent with recent observations that GTP hydrolysis peaks near the dynamin accumulation maximum despite there is a slight, random shift between the two[47]. Such focused GTP hydrolysis possibly indicates that there is a hidden regulation mechanism in vivo that initiates multiple GTP molecules to act in a short time. Interestingly, in the two-state model, all dynamin molecules in adjacent rungs of a helix need to act in a coordinated manner to cut the vesicle neck[11]. Here, we see that the two models and our data are converging. Considering the stepping nature of dynamin sliding on each other in the helix after GTP hydrolysis, it is possible that, once GTP hydrolysis starts, a cascade of reactions follows such that the completion of the earlier reaction triggers the next one until the twist is completed. Thus, the super twist may consist of several steps that appear to be a single large step and the rates of GTP hydrolysis measured in vitro could be much slower than those accomplished in vivo. Note that a defective dynamin in the helix may pause or terminate the cascaded reactions, which is consistent with the observation that a small fraction of defective dynamin substantially decreases the fission activity[11].

We also speculate that the super twist may be paused or terminated in the process. A fraction of successful endocytosis events included a pause then resumed the super twist (for example, 12/45) very quickly (<0.1 s) and scission was completed. In many other cases ($n > 50$), we observed super-twist-like actions that did not result in scission and instead were probably terminated. These observations suggest that, in some cases (>50%), the GTP hydrolysis reactions failed to produce sufficient constriction to drive scission and are consistent with the stochastic nature of dynamin-catalysed scission observed in vitro[12,13]. Interestingly, regardless of whether the super twist continues to complete scission or fails, the accumulated dynamin dissociates. This is possibly an indication that focused GTP hydrolysis is linked to the destabilization of dynamin helix and its disassembly. Nevertheless, the final super twist is indispensable in all of the successful scission events, suggesting that a large torque is the main driving force for scission.

The state of dynamin assembly before and after the super twist. The super twist always occurs near the peak of dynamin accumulation, which is an indication that dynamin recruitment has been completed. An important question is what are the structures of dynamin molecules before and after the twist?

It is generally accepted that assembled dynamin adopts a helical structure before scission but the structure during and after scission

is still under debate. Especially of interest is the super-constricted helix, which has such a small radius (inner dimension, 3.7 nm) that the membrane tube inside can proceed to the hemi-fission intermediate with barely any energy barrier[19,48]. It is tempting to assign the dynamin helix after the super twist as the super-constricted helical state, and dynamin assembly before the super twist as one of the less constricted helices. However, it also has been reported that the super-constricted dynamin helix has a unique two-start structure. Recruiting of additional dynamin and elongation of the membrane tube are required to convert one-start, less constricted helices to the super-constricted state[28]. These observations contributed to the argument that the helices captured in cryo-electron microscopy experiments may not necessarily be on the same pathway leading to scission; other undiscovered intermediates may exist. Yet, it is also possible that they are on the same pathway: the conversion of one-start helix to two-start helix could happen during the cutting, and the super twist could reflect this twisting and tightening process with the insertion of preaccumulated dynamins into the helix. All of these indicate the complexity of the scission process.

Although we are unable to determine the dynamin structures before or after the twist, we speculate that, after the super twist, the dynamin helix is either in a reversible, very constricted state ready for hemi-fission, or, in an irreversible state that has already triggered hemi-fission and partial disassembly of the dynamin helix. After the super twist, a limited increase in rotational freedom (Fig. 6) was observed, yet the vesicle did not leave the endocytosis spot, suggesting that the stable dynamin helix–membrane tube structure has already been broken but the vesicle is still connected to the membrane, possibly through the remaining broken protein scaffold. Complete detachment of the vesicle from the membrane happens at a later time shortly after the super twist (stage E, 2.1 ± 1.4 s; Fig. 4d). The delayed start of active rotation suggests that scission is not an instantaneous action but a gradual process that takes ~1 s to finish.

As a successful super twist always leads to fission and the disassembly of the dynamin assembly, it is more likely that the super twist irreversibly destabilizes the dynamin helical structure due to GTP hydrolysis and induces hemi-fission and partial disassembly of dynamin as suggested by the two-stage model. It is also possible that the super twist tightens the helix and generates conformational stress that breaks the helix as proposed in the ratchet model. As our fluorescence imaging has a limited time resolution (~1 s), we were unable to rule out either of the possibilities. Finally, it is unclear but also possible that more GTP hydrolysis is required in this process to completely sever the connection between the vesicle and the membrane. Other methods will be needed to identify the dynamin helical structures before and after the super twist.

The static period (stage C) before the super twist. The static period, which lasted for 1.9 ± 1.5 s for 40 cases, is another interesting finding (stage C; Fig. 4a). We speculate that the dynamin collar forms around the CCP at this stage so as to limit the fluctuation of membrane and restrict the cargo rotation. The static nature indicates that the dynamin hydrolysis of GTPs did not start immediately but instead the dynamin assembly seemed to wait for a signal to trigger the hydrolysis reaction.

This unexplained phenomenon possibly indicates that GTP hydrolysis by assembled dynamin helix is regulated through an unknown mechanism as also suggested by other groups[47,49,50]. Indeed, there are many processes that occur during scission that are less clear. For example, although the proline-rich domain of dynamin is not required for fission activity in vitro, dynamin's GTPase and fission activities are regulated by SH3 domain proteins that bind to the proline-rich domain[49,50]. Scission is also regulated by BAR-domain proteins such as endophilin and amphiphysin[5,49–52]. Indeed, endophilin, which is recruited in a synchronized manner with dynamin at the late stages of scission[52] and was thought to promote dynamin function[52], has also been shown to inhibit dynamin function at high concentrations[53,54], which may be relevant to the pause of GTPase functionality after dynamin assembly. Another study showed that the stimulatory action of amphiphysin on dynamin is dependent on the curvature of the lipid bilayer[55]. These interactions may be relevant to the paused start of GTPase functionality after dynamin assembly. Or, as an alternative explanation to chemical signalling, the control of GTP hydrolysis may simply be physical—the restoring force from the squeezed membrane tube may stall GTP hydrolysis. Further study is needed to better explain this phenomenon.

In summary, we demonstrated the characteristic translational and rotational motions of the AuNR cargos at different stages throughout the CME process. Especially at the final stage of scission, the dynamin helix induces a large, right-handed twist through coordinated actions from multiple dynamin molecules. This unequivocally shows that a torque is generated in dynamin action in vivo. We summarize the scission model in Fig. 4e, which is consistent with both the ratchet and the two-stage models but provides much missing details regarding dynamin actions in vivo, after which the two models may eventually converge. The rotational study paves the way to a deeper, more comprehensive understanding of how dynamin works by combining other feature studies such as structural characterization and molecular simulations.

Online content

Any methods, additional references, Nature Research reporting summaries, source data, extended data, supplementary information, acknowledgements, peer review information; details of author contributions and competing interests; and statements of data and code availability are available at https://doi.org/10.1038/s41556-021-00713-x.

Received: 6 January 2021; Accepted: 9 June 2021;
Published online: 12 July 2021

References

1. Ferguson, S. M. & De Camilli, P. Dynamin, a membrane-remodelling GTPase. *Nat. Rev. Mol. Cell Biol.* **13**, 75–88 (2012).
2. Kamerkar, S. C., Kraus, F., Sharpe, A. J., Pucadyil, T. J. & Ryan, M. T. Dynamin-related protein 1 has membrane constricting and severing abilities sufficient for mitochondrial and peroxisomal fission. *Nat. Commun.* **9**, 5239 (2018).
3. Koirala, S. et al. Interchangeable adaptors regulate mitochondrial dynamin assembly for membrane scission. *Proc. Natl Acad. Sci. USA* **110**, E1342–E1351 (2013).
4. Yamada, H. et al. Dynasore, a dynamin inhibitor, suppresses lamellipodia formation and cancer cell invasion by destabilizing actin filaments. *Biochem. Biophys. Res. Commun.* **390**, 1142–1148 (2009).
5. Mettlen, M., Chen, P.-H., Srinivasan, S., Danuser, G. & Schmid, S. L. Regulation of clathrin-mediated endocytosis. *Annu. Rev. Biochem.* **87**, 871–896 (2018).
6. Cocucci, E., Gaudin, R. & Kirchhausen, T. Dynamin recruitment and membrane scission at the neck of a clathrin-coated pit. *Mol. Biol. Cell.* **25**, 3595–3609 (2014).
7. Sweitzer, S. M. & Hinshaw, J. E. Dynamin undergoes a GTP-dependent conformational change causing vesiculation. *Cell* **93**, 1021–1029 (1998).
8. Stowell, M. H. B., Marks, B., Wigge, P. & McMahon, H. T. Nucleotide-dependent conformational changes in dynamin: evidence for a mechanochemical molecular spring. *Nat. Cell Biol.* **1**, 27–32 (1999).
9. Roux, A., Uyhazi, K., Frost, A. & De Camilli, P. GTP-dependent twisting of dynamin implicates constriction and tension in membrane fission. *Nature* **441**, 528–531 (2006).
10. Antonny, B. et al. Membrane fission by dynamin: what we know and what we need to know. *EMBO J.* **35**, 2270–2284 (2016).
11. Liu, Y.-W., Mattila, J.-P. & Schmid, S. L. Dynamin-catalyzed membrane fission requires coordinated GTP hydrolysis. *PLoS ONE* **8**, e55691 (2013).
12. Bashkirov, P. V. et al. GTPase cycle of dynamin is coupled to membrane squeeze and release, leading to spontaneous fission. *Cell* **135**, 1276–1286 (2008).
13. Pucadyil, T. J. & Schmid, S. L. Real-time visualization of dynamin-catalyzed membrane fission and vesicle release. *Cell* **135**, 1263–1275 (2008).

14. Shnyrova, A. V. et al. Geometric catalysis of membrane fission driven by flexible dynamin rings. *Science* **339**, 1433–1436 (2013).
15. Mattila, J.-P. et al. A hemi-fission intermediate links two mechanistically distinct stages of membrane fission. *Nature* **524**, 109–113 (2015).
16. Schmid, S. L. & Frolov, V. A. Dynamin: functional design of a membrane fission catalyst. *Annu. Rev. Cell Dev. Biol.* **27**, 79–105 (2011).
17. Chappie, J. S. et al. A pseudoatomic model of the dynamin polymer identifies a hydrolysis-dependent powerstroke. *Cell* **147**, 209–222 (2011).
18. Srinivasan, S., Dharmarajan, V., Reed, D. K., Griffin, P. R. & Schmid, S. L. Identification and function of conformational dynamics in the multidomain GTPase dynamin. *EMBO J.* **35**, 443–457 (2016).
19. Sundborger, A. C. et al. A dynamin mutant defines a superconstricted prefission state. *Cell Rep.* **8**, 734–742 (2014).
20. Kozlovsky, Y. & Kozlov, M. M. Membrane fission: model for intermediate structures. *Biophys. J.* **85**, 85–96 (2003).
21. Morlot, S. et al. Membrane shape at the edge of the dynamin helix sets location and duration of the fission reaction. *Cell* **151**, 619–629 (2012).
22. Colom, A., Redondo-Morata, L., Chiaruttini, N., Roux, A. & Scheuring, S. Dynamic remodeling of the dynamin helix during membrane constriction. *Proc. Natl Acad. Sci. USA* **114**, 5449–5454 (2017).
23. Pannuzzo, M., McDargh, Z. A. & Deserno, M. The role of scaffold reshaping and disassembly in dynamin driven membrane fission. *eLife* **7**, e39441 (2018).
24. Takei, K. et al. Generation of coated intermediates of clathrin-mediated endocytosis on protein-free liposomes. *Cell* **94**, 131–141 (1998).
25. Takei, K., Slepnev, V. I., Haucke, V. & De Camilli, P. Functional partnership between amphiphysin and dynamin in clathrin-mediated endocytosis. *Nat. Cell Biol.* **1**, 33–39 (1999).
26. Danino, D., Moon, K. H. & Hinshaw, J. E. Rapid constriction of lipid bilayers by the mechanochemical enzyme dynamin. *J. Struct. Biol.* **147**, 259–267 (2004).
27. Zhang, P. & Hinshaw, J. E. Three-dimensional reconstruction of dynamin in the constricted state. *Nat. Cell Biol.* **3**, 922–926 (2001).
28. Kong, L. et al. Cryo-EM of the dynamin polymer assembled on lipid membrane. *Nature* **560**, 258–262 (2018).
29. Willets, K. A. & Van Duyne, R. P. Localized surface plasmon resonance spectroscopy and sensing. *Annu. Rev. Phys. Chem.* **58**, 267–297 (2007).
30. Cheng, X. et al. Resolving cargo-motor-track interactions with bifocal parallax single-particle tracking. *Biophys. J.* **120**, 1378–1386 (2021).
31. Qian, Z. M., Li, H., Sun, H. & Ho, K. Targeted drug delivery via the transferrin receptor-mediated endocytosis pathway. *Pharmacol. Rev.* **54**, 561–587 (2002).
32. Gu, Y. et al. Rotational dynamics of cargos at pauses during axonal transport. *Nat. Commun.* **3**, 1030 (2012).
33. Chen, K. et al. Characteristic rotational behaviors of rod-shaped cargo revealed by automated five-dimensional single particle tracking. *Nat. Commun.* **8**, 887 (2017).
34. Kaplan, L., Ierokomos, A., Chowdary, P., Bryant, Z. & Cui, B. Rotation of endosomes demonstrates coordination of molecular motors during axonal transport. *Sci. Adv.* **4**, e1602170 (2018).
35. Cureton, D. K., Massol, R. H., Whelan, S. P. J. & Kirchhausen, T. The length of vesicular stomatitis virus particles dictates a need for actin assembly during clathrin-dependent endocytosis. *PLoS Pathog.* **6**, e1001127 (2010).
36. Xiao, L., Ha, J. W., Wei, L., Wang, G. & Fang, N. Determining the full three-dimensional orientation of single anisotropic nanoparticles by differential interference contrast microscopy. *Angew. Chem. Int.* **51**, 7734–7738 (2012).
37. Grassart, A. et al. Actin and dynamin2 dynamics and interplay during clathrin-mediated endocytosis. *J. Cell Biol.* **205**, 721–735 (2014).
38. Gu, Y., Sun, W., Wang, G. & Fang, N. Single particle orientation and rotation tracking discloses distinctive rotational dynamics of drug delivery vectors on live cell membranes. *J. Am. Chem. Soc.* **133**, 5720–5723 (2011).
39. Gu, Y. et al. Revealing rotational modes of functionalized gold nanorods on live cell membranes. *Small* **9**, 785–792 (2013).
40. Taylor, M. J., Perrais, D. & Merrifield, C. J. A high precision survey of the molecular dynamics of mammalian clathrin-mediated endocytosis. *PLoS Biol.* **9**, e1000604 (2011).
41. Merrifield, C. J., Perrais, D. & Zenisek, D. Coupling between clathrin-coated-pit invagination, cortactin recruitment, and membrane scission observed in live cells. *Cell* **121**, 593–606 (2005).
42. Engqvist-Goldstein, Å. E. & Drubin, D. G. Actin assembly and endocytosis: from yeast to mammals. *Annu. Rev. Cell Dev. Biol.* **19**, 287–332 (2003).
43. Boulant, S., Kural, C., Zeeh, J.-C., Ubelmann, F. & Kirchhausen, T. Actin dynamics counteract membrane tension during clathrin-mediated endocytosis. *Nat. Cell Biol.* **13**, 1124–1131 (2011).
44. Kaksonen, M. & Roux, A. Mechanisms of clathrin-mediated endocytosis. *Nat. Rev. Mol. Cell Biol.* **19**, 313 (2018).
45. Chen, Y.-J., Zhang, P., Egelman, E. H. & Hinshaw, J. E. The stalk region of dynamin drives the constriction of dynamin tubes. *Nat. Struct. Mol. Biol.* **11**, 574–575 (2004).
46. Chappie, J. S., Acharya, S., Leonard, M., Schmid, S. L. & Dyda, F. G domain dimerization controls dynamin's assembly-stimulated GTPase activity. *Nature* **465**, 435–440 (2010).
47. Galli, V., Sebastian, R., Moutel, S., Ecard, J. & Roux, A. Uncoupling of dynamin polymerization and GTPase activity revealed by the conformation-specific nanobody dynab. *eLife* **6**, e25197 (2017).
48. Jimah, J. R. & Hinshaw, J. E. Structural insights into the mechanism of dynamin superfamily proteins. *Trends Cell Biol.* **29**, 257–273 (2019).
49. Meinecke, M. et al. Cooperative recruitment of dynamin and BIN/amphiphysin/Rvs (BAR) domain-containing proteins leads to GTP-dependent membrane scission. *J. Biol. Chem.* **288**, 6651–6661 (2013).
50. Neumann, S. & Schmid, S. L. Dual role of BAR domain-containing proteins in regulating vesicle release catalyzed by the GTPase dynamin-2. *J. Biol. Chem.* **288**, 25119–25128 (2013).
51. Daumke, O., Roux, A. & Haucke, V. BAR domain scaffolds in dynamin-mediated membrane fission. *Cell* **156**, 882–892 (2014).
52. Haucke, V. & Kozlov, M. M. Membrane remodeling in clathrin-mediated endocytosis. *J. Cell Sci.* **131**, 17 (2018).
53. Boucrot, E. et al. Membrane fission is promoted by insertion of amphipathic helices and is restricted by crescent BAR domains. *Cell* **149**, 124–136 (2012).
54. Hohendahl, A. et al. Structural inhibition of dynamin-mediated membrane fission by endophilin. *eLife* **6**, e26856 (2017).
55. Yoshida, Y. et al. The stimulatory action of amphiphysin on dynamin function is dependent on lipid bilayer curvature. *EMBO J.* **23**, 3483–3491 (2004).

Publisher's note Springer Nature remains neutral with regard to jurisdictional claims in published maps and institutional affiliations.

© The Author(s), under exclusive licence to Springer Nature Limited 2021

Methods

Mutlidimensional microscopy. A Nikon Eclipse 80i upright microscope equipped with a heating stage (Bioscience Tools) was used in this study. For dark-field microscopy, a Nikon oil-immersion dark-field condenser (numerical aperture (NA), 1.20–1.43) and a Nikon ×60 Plan Fluor oil-immersion objective (NA, 0.5–1.25) were used with the NA set to 1.0. The same objective was used for both excitation and emission collection. The scattering of gold nanoparticles was excited using a transmission light from a halogen lamp that is filtered with a band-pass filter (FF01-650/13, Semrock). The fluorescence of GFP–dynamin2 and RFP–CLTA was excited using two collimated and coaligned 488 nm (50 mW) and 561 nm (100 mW) lasers (Oxxius), which were reflected into the collecting objective by a dual-band dichroic mirror (Di03-R488/561, Semrock). A dual-band pass filter (FF01-482/563, Semrock) in front of the dichroic mirror was used to clean up the two lasers. To reduce the fluorescence background, variable angle epifluorescence illumination configuration was used. Both illumination pathways (dark-field scattering and fluorescence) were turned on at the same time in multidimensional imaging experiments.

Simultaneous dark-field scattering and fluorescence imaging were achieved using a self-designed and custom-made four-channel imaging module (Fig. 1). In brief, the fluorescence and dark-field signals were collected simultaneously through the same objective and relayed to the four-channel imaging module for further splitting and processing. To remove the scattering background from the lasers, a combination of two notch filters (ZET488NF and ZET561NF, Chroma) was used before entering the four-channel imaging module. The collected signals were first split by a long-pass dichroic mirror (BLP01-635R, Semrock): reflection for fluorescence (left arm) and transmission for dark-field scattering (right arm). The reflected fluorescence signals were further split into two channels using a long-pass dichroic mirror (LP03-532RU, Semrock). Fluorescence signals of dynamin and clathrin in each channel were filtered using two band-pass filters FF01-512/25 (Semrock) and FF01-598/25 (Semrock), respectively. Both channels of the fluorescence images were then focused to different portions of a same EMCCD camera chip (Andor Technology; iXonEM+ Ultra 888) through the same left exit port of the imaging module. Bifocal imaging, parallax microscopy and the auto-chasing under dark-field mode were achieved in the right arm of the four-channel imaging module. First, the dark-field image was split into a focused channel and a defocused channel using a beam splitter (Thorlabs) whereby 30% of signal was in the focused channel for localization and auto-chasing and 70% of signal was in the defocused channel for orientation determination. In the defocused channel, an additional focal lens (f = 500 mm) was inserted into the optical pathway to create a defocusing distance of 0.9 μm, which was found to generate the most suitable defocused image patterns for orientation determination. The dark-field images in focused and defocused channels were focused to different portions of a second EMCCD camera (Andor Technology; iXonEM+ Ultra 897) through the same right exit port of the four-channel imaging module.

All dark-field videos were recorded at 50 frames per second (f.p.s.). The heating stage was set to 37 °C to maintain the living conditions for cells. Fluorescence images were recorded at 1 f.p.s. or 0.5 f.p.s. The image acquisition on two EMCCD cameras were triggered and synchronized using a mechanical shutter. The acquired images were analysed using ImageJ and MATLAB.

3D-SPORT. Bifocal imaging, parallax microscopy and an automatic feedback control module are the key components of the imaging system. The purpose of the design is to keep the target probe in focus continuously in the focused channel to extract the 3D spatial coordinates (x, y, z) with nanoscale precision while obtaining image patterns with a constant defocusing distance in the defocused channel to determine the probe's orientation angles accurately and robustly.

The auto-chasing was achieved using parallax imaging in the focused channel. In brief, a custom-cut wedge prism (0.5°, Edmund) was inserted into the focused channel near the back focal plane of the objective to deviate half of the scattering light from the sample by a very small angle, effectively splitting the light to form two half-plane images (as opposed to the standard full-plane images using the full pupil) in only the focused channel. The two associated half-plane mirror images for a single probe are always manually aligned vertically, and they are referred to as the upper and lower image, respectively, throughout our discussions. The x and y coordinates were resolved by Gaussian fitting. The z position of a probe is a function of the separation distance (Δy) between its upper and lower images. A calibration curve was constructed experimentally to correlate this relationship. The experimental localization precision in the x, y and z axes (Extended Data Fig. 1) is 4.9 nm, 6.3 nm and 14.0 nm, respectively. Finally, the automatic feedback control system, composed of a piezo objective scanner (Physik Instrumente) and a tracking program in μManger, was implemented to keep the target probe in focus. When the target probe was in perfect focus, the y distance between the upper and lower images in the focused channel was obtained as the reference (Δy_0). During the tracking, Δy was calculated for every other frame. The tracking program would move the objective scanner to keep the target probe in focus in the next frame.

Preparation of surface-modified AuNRs for cell experiments. Sodium citrate-capped AuNRs (40 nm × 80 nm) were purchased from Nanopartz. The average aspect ratio of the AuNRs is 2.0. The electrostatic adsorption method establishing transferrin-coated AuNRs was used according to a published method[30]. In brief, 100 μl of the AuNRs solution (3.7×10^{10} ml^{-1}) was mixed with 4 μl of 50 mM borate buffer (pH 8.5). Then 5 μl of 3 mg ml^{-1} transferrin (11096-37-0, Sigma-Aldrich) was added to the AuNR solution and reacted for 3 h. Finally, the mixture was centrifuged at 5,000 r.p.m. for 5 min twice and resuspended in 100 μl of 2 mM borate buffer (pH 8.5). AuNRs modified this way were shown to be up taken by cells predominantly through the CME pathway (more than ~70%)[31,32].

Cell culture. The A549 human lung cancer cell line was purchased from American Type Culture Collection (ATCC, CCL-185). The SK-MEL-2 cell line was a gift from the Drubin group (UC Berkeley). The cells were cultured in a T25 cell culture flask (Corning) and grown in cell culture medium (DMEM/F12, Gibco) supplemented with 10% fetal bovine serum (FBS). This cell culture medium contains both ferric nitrate and ferrous sulfate. When subculturing, 150 μl of cell suspension solution was transferred to a 22 × 22 mm coated coverslip, housed in a 35 mm Petri dish (Corning). Next, 1.5 ml of the cell culture medium with 10% FBS supplement was added to immerse the coverslip, the Petri dish was kept in the incubator for 48 h.

Transfection of A549 cells to express GFP–DNM2^{K44A}. *E. Coli* bacteria with GFP–DNM2^{K44A} plasmid was purchased from Addgene (plasmid 22301). The plasmid was purified from the bacteria using the plasmid extraction kit (27104). The high-density A549 cells were subcultured on a coverslip in a Petri dish in the incubator. After 24 h, the GFP–DNM2^{K44A} was mixed with Lipofectamine 3000 regent in the Opti-EME medium (Thermo Fisher Scientific) first and then added to the Petri dish. After incubation for 48 h, the cells were ready for imaging.

Quantification of AuNR internalization. The wild-type A549 cells and A549 cells expressing GFP–DNM2^{K44A} were cultured on a coverslip in Petri dishes overnight in the incubator. Then, AuNRs functionalized with transferrin were injected into the Petri dish and the final concentration of AuNRs was 3.7×10^9 ml^{-1}. After incubation for 2 h in the incubator, the cells were ready to be used. The uptake of AuNRs was visualized using a DIC microscope at 650 nm wavelength and z stacks were obtained using an objective scanner and reconstructed using ImageJ. Next, the endocytosed AuNRs in individual cells were identified and counted. The counted numbers of AuNRs per cell in A549 cells expressing GFP–DNM2^{K44A} and wild-type A549 cells were 2.0 ± 1.0 (mean ± s.d.; n = 20, biologically independent experiments) and 11.4 ± 4.4 (mean ± s.d.; n = 20, biologically independent experiments), respectively.

Live-cell imaging of endocytosis. Two pieces of double-sided tape were adhered to the clean glass side. A cover glass with adherent cells was placed on the top of the double-sided tape with cells facing the glass slide, to form a chamber. Then, 5 μl of the transferrin@AuNRs solution mixed with 45 μl of the cell culture medium was injected into the chamber. To prevent evaporation and leakage of the medium, the cover glass was sealed with nail polish.

Statistics and reproducibility. All results are expressed as either absolute values or mean ± s.d. P values were calculated using unpaired two-tailed Student's t-tests with unequal variance for comparison of two groups. Exact P values are provided in the legends when available. Asterisks indicate significant differences; $^{***}P < 0.001$. No sample size calculation was performed. Sample size was determined on the basis of our experience and previous studies. All data were replicated at least three times and most results were representative of ten or more times in independent experiments with similar results obtained.

Reporting Summary. Further information on research design is available in the Nature Research Reporting Summary linked to this article.

Data availability

Source data are provided with this paper. All other data supporting the findings of this study are available from the corresponding authors on reasonable request.

Code availability

The auto-chasing was achieved using Micro-Manager. The localization and orientation of an AuNR was analysed with MATLAB. All code is available from the corresponding authors on request.

Acknowledgements

We thank D. Drubin for providing the gene-edited SK-MEL-2 cell line, and S. Schmid for insightful comments and help during the completion of this manuscript. This work is supported by National Institution of Health (R01GM115763). X.C. acknowledges partial support from Science and Technology Projects of Innovation Laboratory for Sciences and Technologies of Energy Materials of Fujian Province (IKKEM) (RD2020050501).

Author contributions

X.C., K.C. and B.D. contributed equally to this work. G.W. and N.F. conceived the idea. X.C., K.C., B.D., G.W. and N.F. designed the research. X.C., K.C. and B.D. built the

imaging setup. M.Y., S.L.F., Y.M., T.-X.H. and Y.G. contributed to the experiments. All of the authors performed the experiments and wrote the manuscript.

Competing interests
The authors declare no competing interests.

Additional information
Extended data is available for this paper at https://doi.org/10.1038/s41556-021-00713-x.

Supplementary information The online version contains supplementary material available at https://doi.org/10.1038/s41556-021-00713-x.

Correspondence and requests for materials should be addressed to G.W. or N.F.

Peer review information *Nature Cell Biology* thanks Sandra Schmid, Aurélien Roux and the other, anonymous, reviewer(s) for their contribution to the peer review of this work. Peer reviewer reports are available.

Reprints and permissions information is available at www.nature.com/reprints.

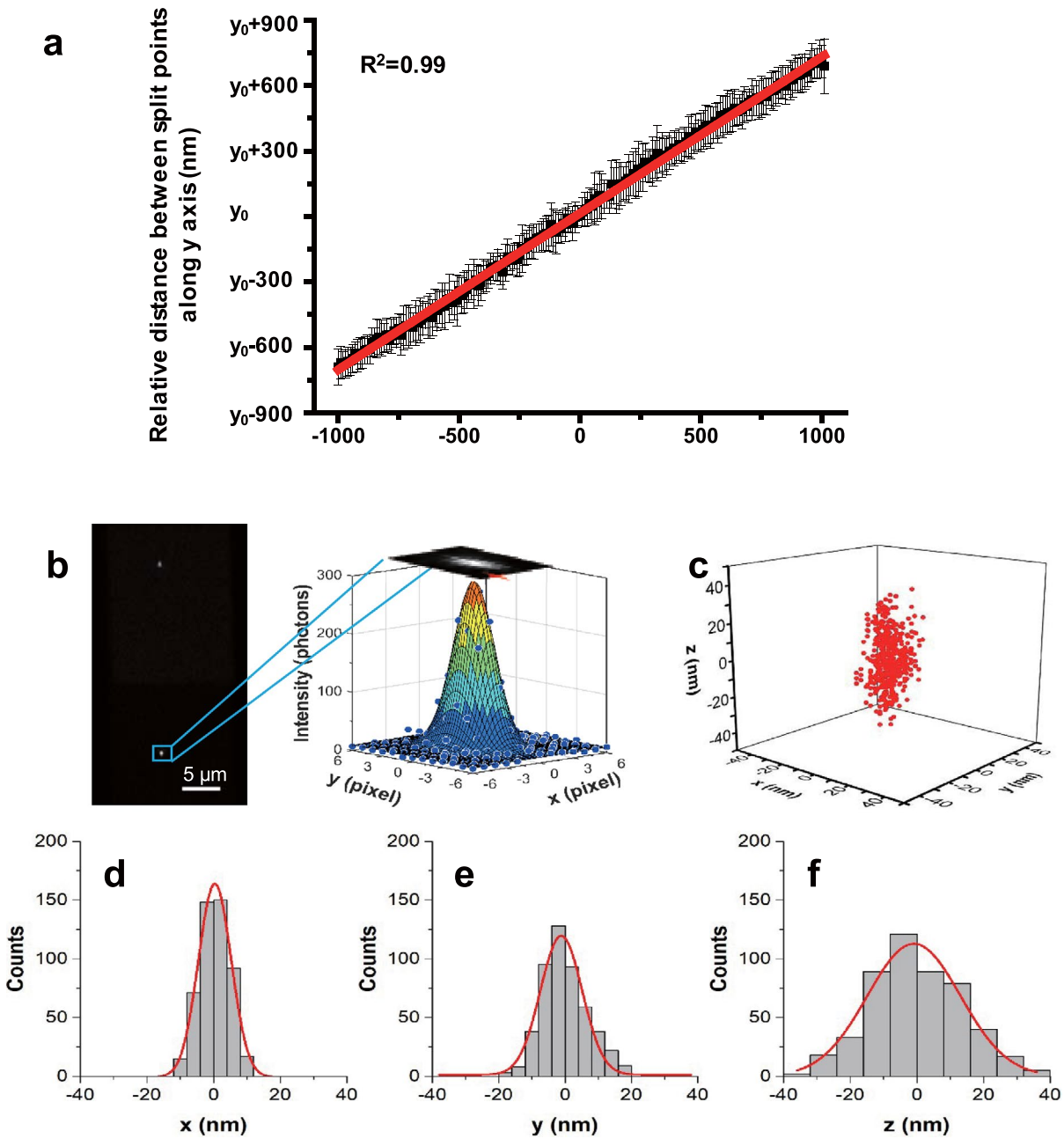

Extended Data Fig. 1 | Calibration curve of Δy *vs.* Δz and 3D localization precision of a AuNR. a, The AuNRs were immobilized on a glass slide surface with various orientations and scanned along the z-axis from -1000 nm to 1000 nm with 10 nm steps using a high-precision objective scanner (Data were expressed as mean ± SD, n = 20 independent experiments). **b**, Typical upper and lower half-plane dark-field images of a AuNR with 0.02 s integration time are shown on the left. Scale bar is 5 μm. The lateral positions of the AuNR are determined by 2D elliptical Gaussian fitting (right) the intensity profile. **c**, Scatter plot of locations of the same AuNR in 500 frames. The x, y positions are determined using 2D elliptical Gaussian fitting of the particle image intensity profile. The z positions are obtained from feedback of the objective scanner when auto-focusing system was engaged. The localization precision is determined as the standard deviation from 1D Gaussian function fitting the histogram distribution of the AuNR locations in x, y, z, giving $\sigma_x = 4.9$ nm (**d**), $\sigma_y = 6.3$ nm (E) and $\sigma_z = 14.0$ nm (**f**).

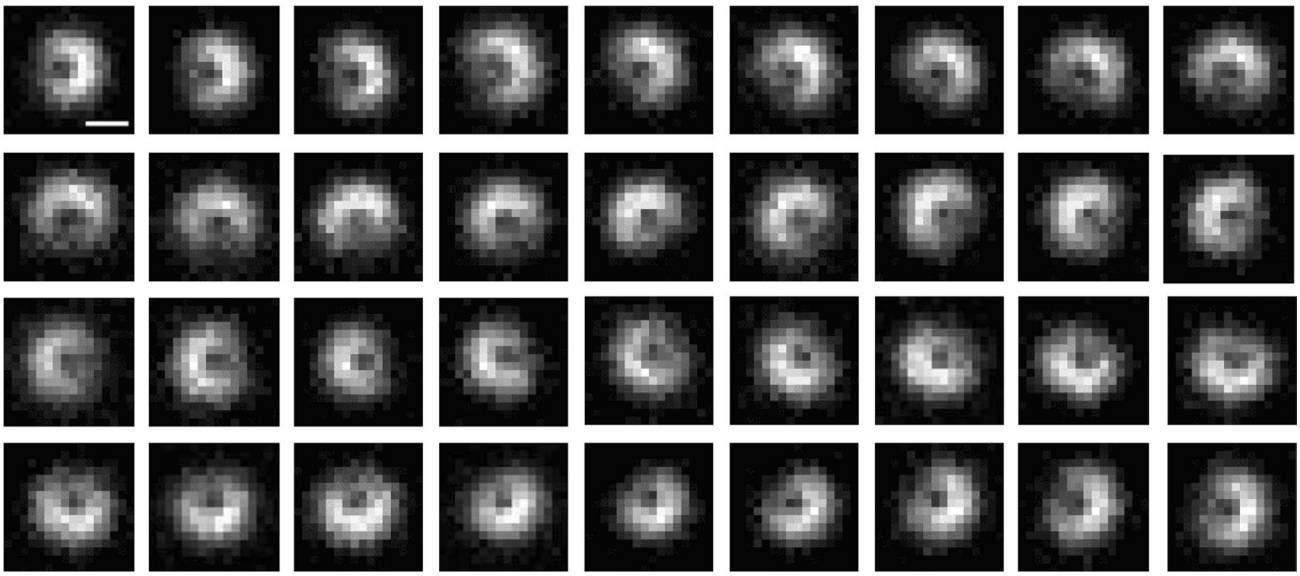

Extended Data Fig. 2 | Another example of the full plane defocused image patterns of a AuNR. The defocused images of a AuNR with a polar angle of 60° at different azimuth angles with 10° intervals were shown. Scale bar is 1 μm.

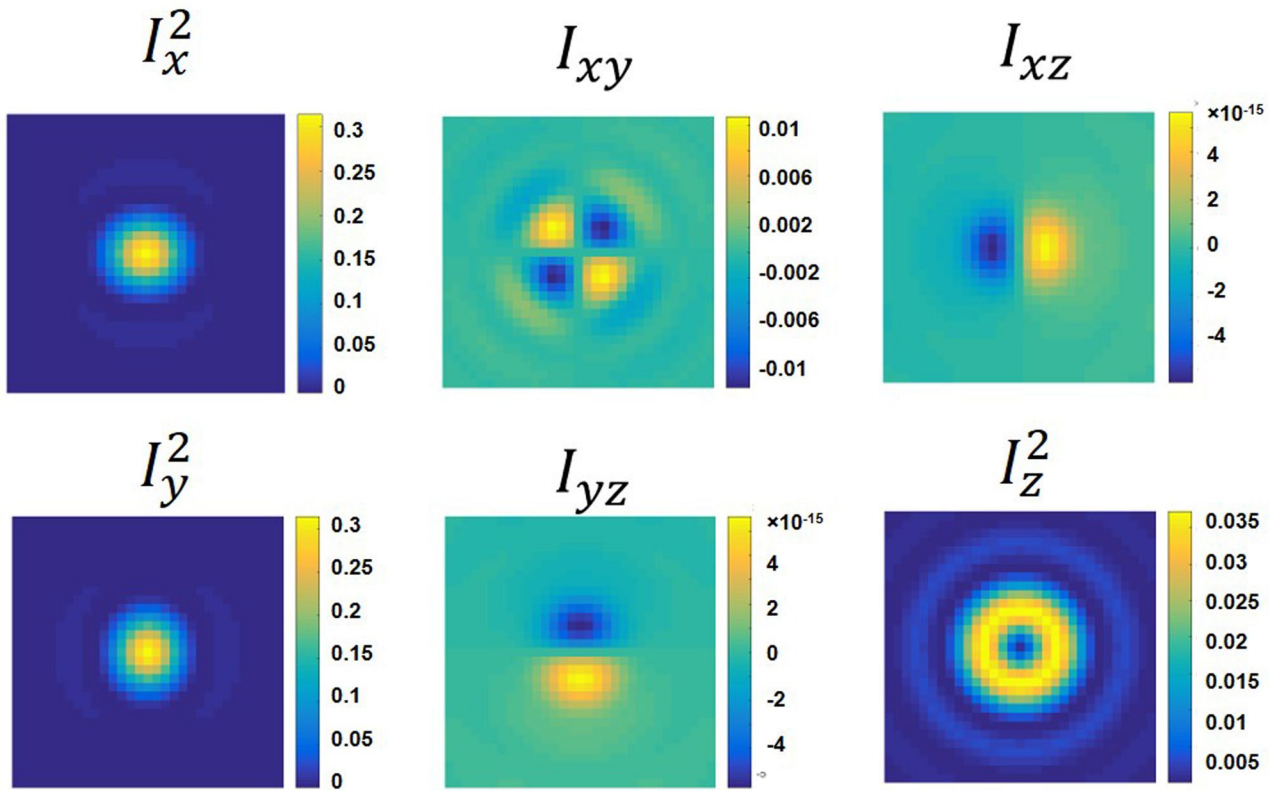

Extended Data Fig. 3 | The six basic dipole emission templates used in simulation. These basic image patterns are dependent on system-specific parameters including the numerical aperture and magnification of the objective, and the defocusing distance.

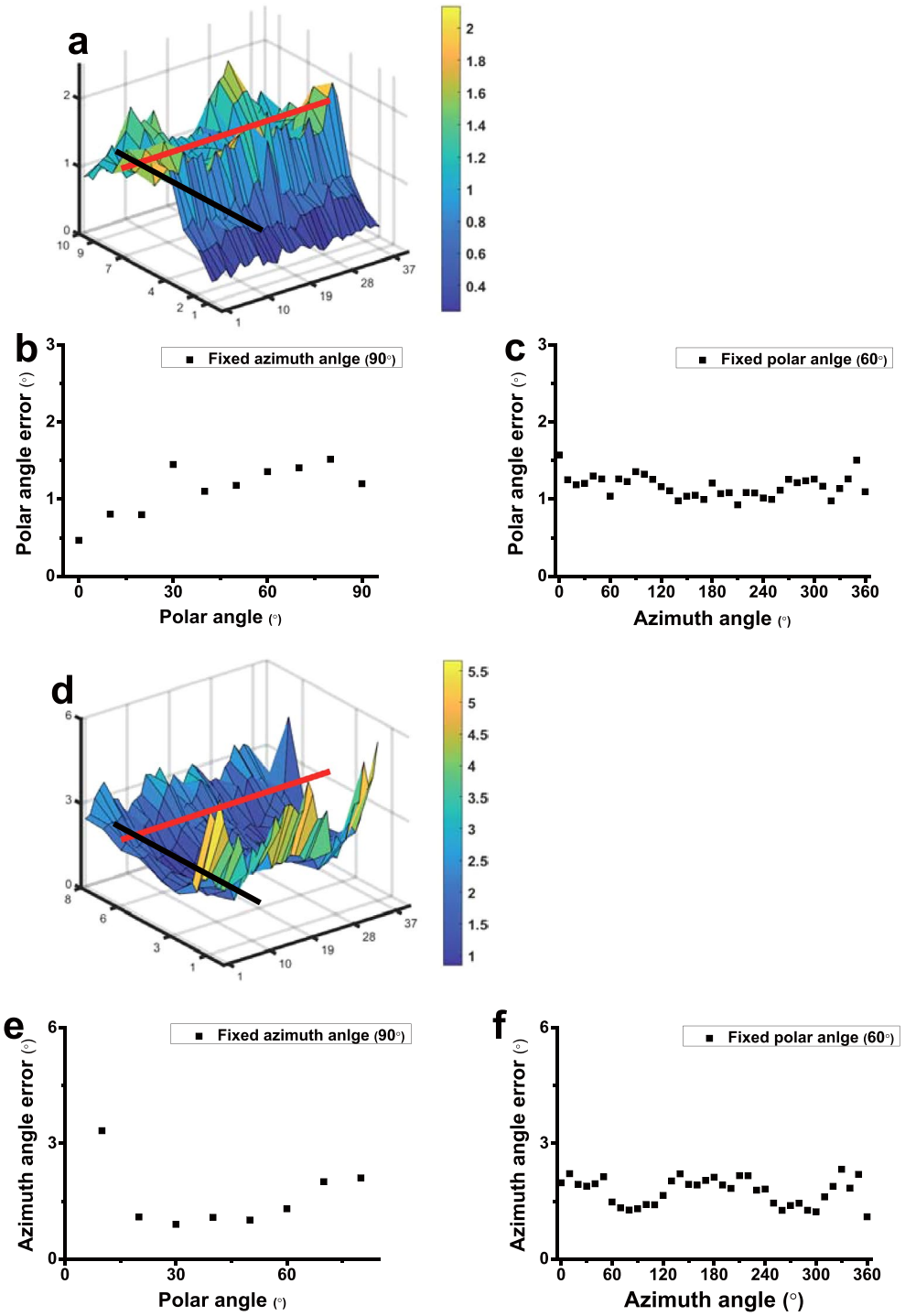

Extended Data Fig. 4 | Estimated polar and azimuth angle errors for orientation recovery at S/N = 10. a, Estimated polar errors for orientation with various combinations of the azimuth angle and polar angle at S/N = 10. **b**, The cross section along the black line in (**a**) shows the polar angle errors with various polar angles and a fixed azimuth angle of 90°. **c**, The cross section along the red line in (**a**) represents the polar angle errors with various azimuth angles and a fixed polar angle of 60°. **d**, Estimated azimuth errors for orientation with various combinations of the azimuth angle and polar angle at S/N = 10. **e**, The cross section along the black line in (**d**) shows the azimuth angle errors with various polar angles and a fixed azimuth angle of 90°. **f**, The cross section along the red line in (**d**) represents the azimuth angle errors with various azimuth angles and a fixed polar angle of 60°.

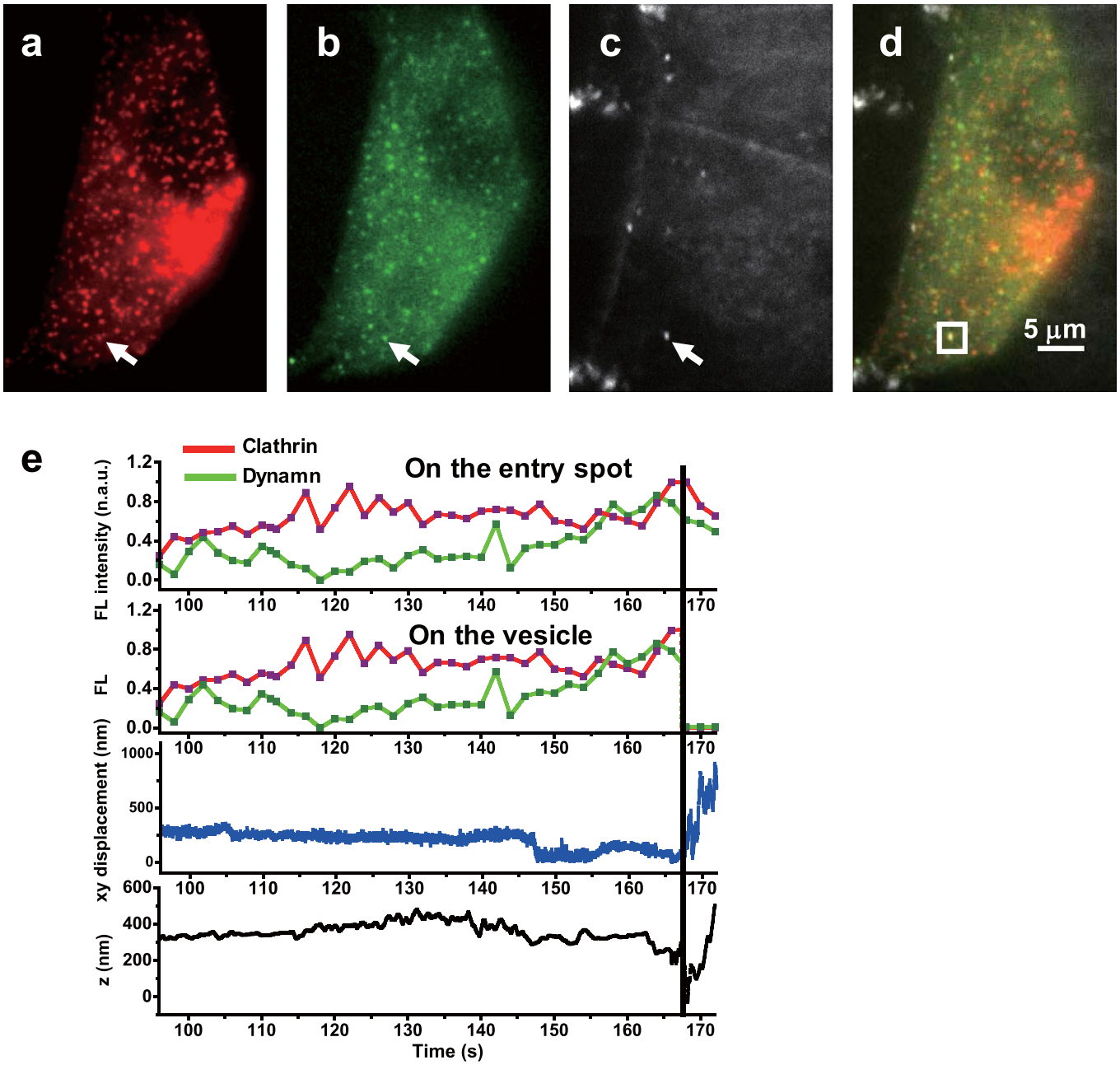

Extended Data Fig. 5 | Dynamin and clathrin fluorescence during endocytosis of the example shown in Fig. 3. a, Clathrin channel. **b**, Dynamin channel. **c**, Focused scattering channel for AuNRs. **d**, Overlapped images. **e**, Time evolution of clathrin and dynamin fluorescence on the entry spot, clathrin and dynamin fluorescence on the vesicle, the xy-, and the z-displacement of the particle from the entry spot during an endocytosis event. The dashed line indicates the time of fission point. The experiments have been performed 5 times and with similar results obtained.

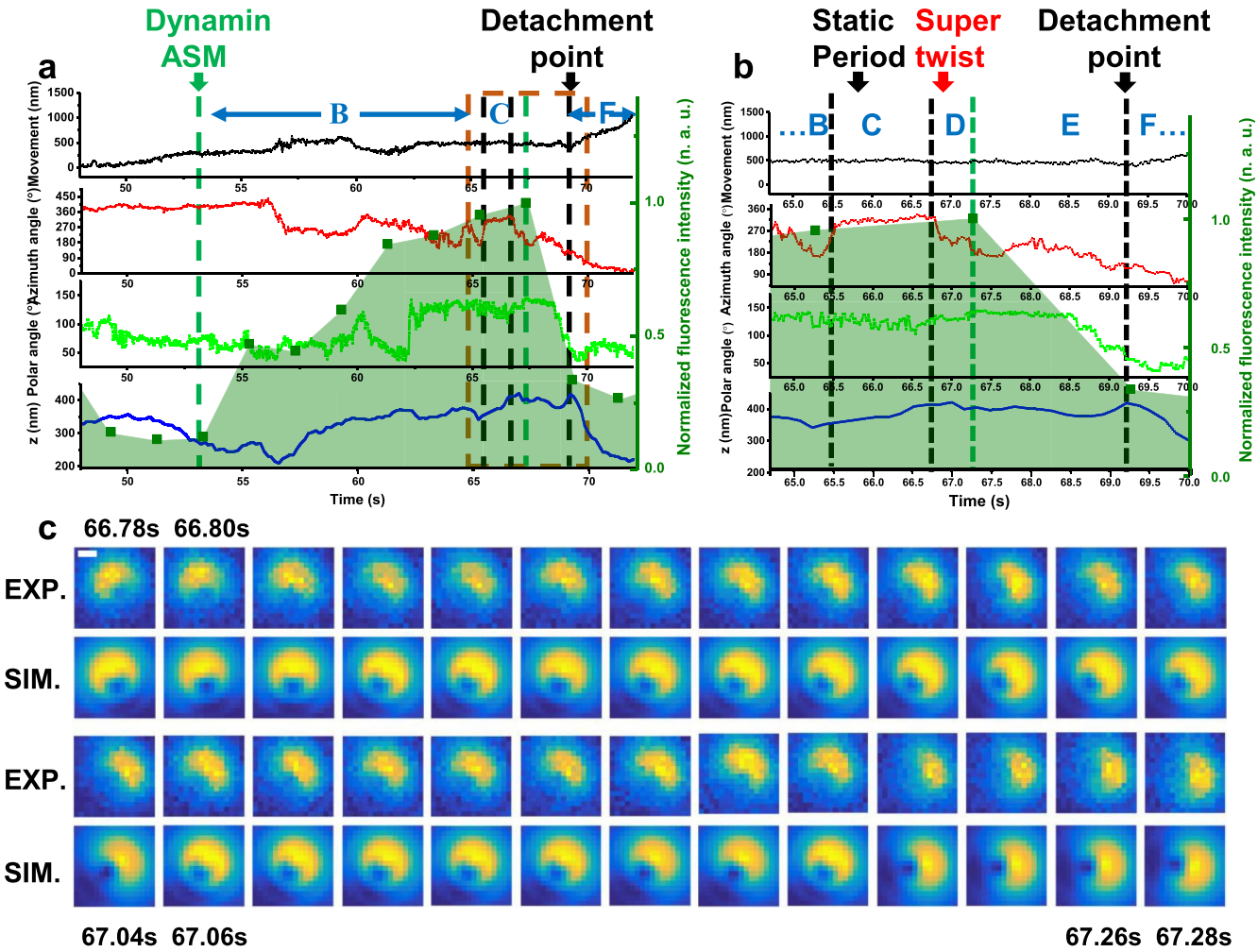

Extended Data Fig. 6 | A complete 3D trajectory, rotation information, and dynamin fluorescence of an endocytosis event. a, The overlay of the time evolution of the cargo's xy-, z-displacements, rotational azimuth and polar angles, and dynamin fluorescence in the background, respectively. Labels B, C, D, E and F represent various stages during the endocytosis. **b**, Expanded time window near the fission point (orange frame) in (**a**). **c**, Cargo's defocused image patterns showing the "super twist" at Stage D. The scale bar is 500 nm. The experiments have been performed 45 times, with similar results obtained.

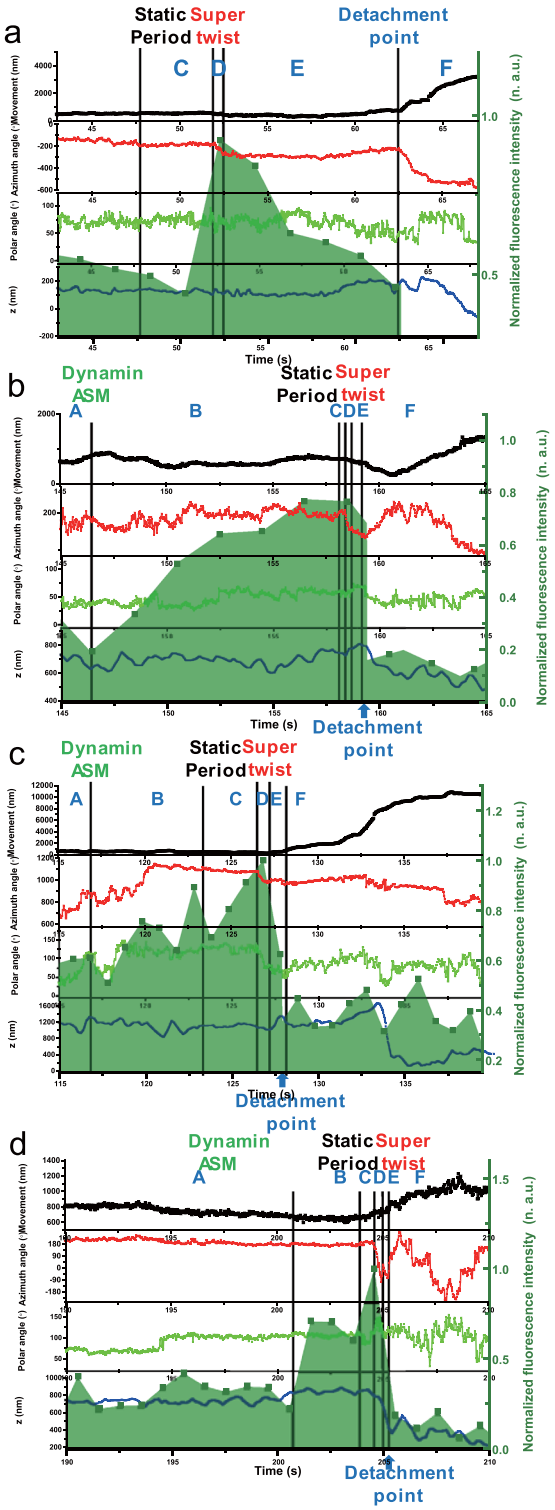

Extended Data Fig. 7 | More examples of complete endocytosis events. a, Example 1, **b**, Example 2, **c**, Example 3 and **d**, Example 4. The overlay of the time evolution of the cargo's xy-, z-displacements, rotational azimuth and polar angles, and dynamin fluorescence in the background, respectively. Labels A, B, C, D, E, and F represent various stages during endocytosis.

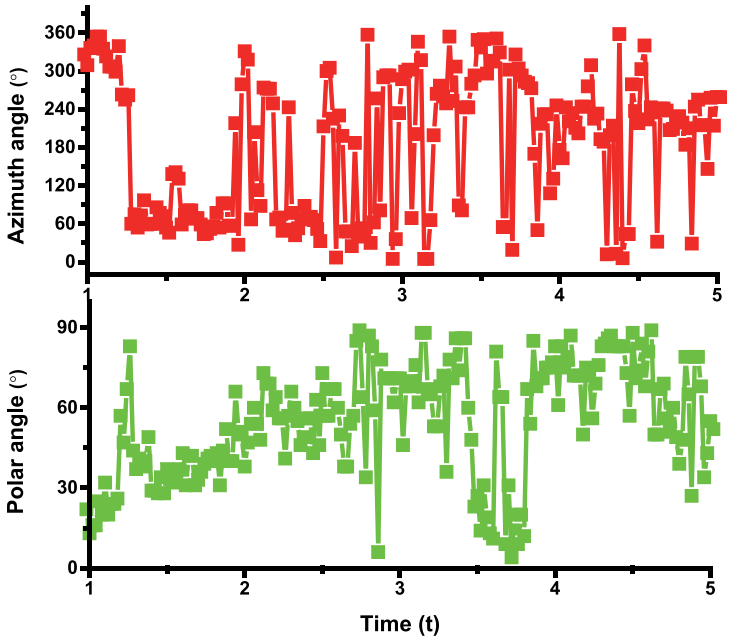

Extended Data Fig. 8 | An example of rotational tracking of a AuNR in Stage a. The overlay of the time evolution of the cargo rotational azimuth, and polar angles in stage a. The experiments have been performed 45 times and with similar results obtained.

nature research

Corresponding author(s): Ning Fang

Last updated by author(s): May 21, 2021

Reporting Summary

Nature Research wishes to improve the reproducibility of the work that we publish. This form provides structure for consistency and transparency in reporting. For further information on Nature Research policies, see our Editorial Policies and the Editorial Policy Checklist.

Statistics

For all statistical analyses, confirm that the following items are present in the figure legend, table legend, main text, or Methods section.

n/a	Confirmed	
☐	☒	The exact sample size (*n*) for each experimental group/condition, given as a discrete number and unit of measurement
☐	☒	A statement on whether measurements were taken from distinct samples or whether the same sample was measured repeatedly
☐	☒	The statistical test(s) used AND whether they are one- or two-sided *Only common tests should be described solely by name; describe more complex techniques in the Methods section.*
☒	☐	A description of all covariates tested
☒	☐	A description of any assumptions or corrections, such as tests of normality and adjustment for multiple comparisons
☐	☒	A full description of the statistical parameters including central tendency (e.g. means) or other basic estimates (e.g. regression coefficient) AND variation (e.g. standard deviation) or associated estimates of uncertainty (e.g. confidence intervals)
☐	☒	For null hypothesis testing, the test statistic (e.g. *F*, *t*, *r*) with confidence intervals, effect sizes, degrees of freedom and *P* value noted *Give P values as exact values whenever suitable.*
☒	☐	For Bayesian analysis, information on the choice of priors and Markov chain Monte Carlo settings
☒	☐	For hierarchical and complex designs, identification of the appropriate level for tests and full reporting of outcomes
☒	☐	Estimates of effect sizes (e.g. Cohen's *d*, Pearson's *r*), indicating how they were calculated

Our web collection on statistics for biologists contains articles on many of the points above.

Software and code

Policy information about availability of computer code

Data collection	Solis (Andor Technology) and Micro-Manager 1.4.18 were used to acquire images.
Data analysis	ImageJ 1.52n was used to analysis and combine the fluorescence and scattering images from multichannel imaging system. Matlab 2016a were used to resolve the localization and orientation of gold nanorods.

For manuscripts utilizing custom algorithms or software that are central to the research but not yet described in published literature, software must be made available to editors and reviewers. We strongly encourage code deposition in a community repository (e.g. GitHub). See the Nature Research guidelines for submitting code & software for further information.

Data

Policy information about availability of data

All manuscripts must include a data availability statement. This statement should provide the following information, where applicable:

- Accession codes, unique identifiers, or web links for publicly available datasets
- A list of figures that have associated raw data
- A description of any restrictions on data availability

We have uploaded the source data for all figures.
All other data supporting the findings of this study are available from the corresponding author on reasonable request.

Field-specific reporting

Please select the one below that is the best fit for your research. If you are not sure, read the appropriate sections before making your selection.

☒ Life sciences ☐ Behavioural & social sciences ☐ Ecological, evolutionary & environmental sciences

For a reference copy of the document with all sections, see nature.com/documents/nr-reporting-summary-flat.pdf

Life sciences study design

All studies must disclose on these points even when the disclosure is negative.

Sample size	No sample size calculation was performed. Sample size was determined based on our experience and previous studies. For experiments involving observing the endocytic events at single-particle level, n>40 was chosen as the minimal replicate number. The sample size was determined by the number of successful endocytic events for the single gold nanorod. For other experiments, All results were replicated at least three times and most ten or more times in independent experiments.
Data exclusions	Data were not excluded from the analysis.
Replication	All results were replicated at least three times and most ten or more times in independent experiments, with similar results obtained
Randomization	The allocation of experimental cells into groups was random. For cell culture, cells were seeded and cultured equally. For imaging experiments, the cells on the cover glass were randomly selected and the imaging field of a single cell were also randomly selected.
Blinding	Comparison between mutant type cells and wild type cells were not performed in a blinded manner as the researcher need to know the difference to accomplish the study. All data were acquired and analyzed with a standard method to resolve the orientation, thus, blinding was not related to the study.

Reporting for specific materials, systems and methods

We require information from authors about some types of materials, experimental systems and methods used in many studies. Here, indicate whether each material, system or method listed is relevant to your study. If you are not sure if a list item applies to your research, read the appropriate section before selecting a response.

Materials & experimental systems

n/a	Involved in the study
☒	☐ Antibodies
☐	☒ Eukaryotic cell lines
☒	☐ Palaeontology and archaeology
☒	☐ Animals and other organisms
☒	☐ Human research participants
☒	☐ Clinical data
☒	☐ Dual use research of concern

Methods

n/a	Involved in the study
☒	☐ ChIP-seq
☒	☐ Flow cytometry
☒	☐ MRI-based neuroimaging

Eukaryotic cell lines

Policy information about cell lines

Cell line source(s)	A549 human lung cancer cell line was purchased from American Type Culture Collection (ATCC, Manassas, VA; catalog number: CCL-185). SK-MEL-2 cell line was a gift from the David Drubin group (UC Berkeley).
Authentication	Cell lines were not authenticated.
Mycoplasma contamination	Cell lines were testd negative for mycoplasma contamination with MycoFluor Mycoplasma Detection Kit (M-7006).
Commonly misidentified lines (See ICLAC register)	No commonly misidentified cell lines were used.